Meteoritics & Planetary Science 36, 1673–1695 (2001)
Available online at http://www.uark.edu/meteor

X-ray fluorescence measurements of the surface elemental composition of asteroid 433 Eros

LARRY R. NITTLER[1†*], RICHARD D. STARR[2], LUCY LIM[3], TIMOTHY J. MCCOY[4], THOMAS H. BURBINE[4], ROBERT C. REEDY[5], JACOB I. TROMBKA[1], PAUL GORENSTEIN[6], STEVEN W. SQUYRES[3], WILLIAM V. BOYNTON[7], TIMOTHY P. MCCLANAHAN[1], JESSE S. BHANGOO[7], PAMELA E. CLARK[2], MARY ELLEN MURPHY[2‡] AND ROSEMARY KILLEN[8]

[1]Goddard Space Flight Center, Code 691, Greenbelt, Maryland 20771, USA
[2]The Catholic University of America, Physics Department, 620 Michigan Avenue Northeast, Washington, D.C. 20064, USA
[3]Cornell University, Space Sciences Building, Ithaca, New York 14853, USA
[4]Department of Mineral Sciences, National Museum of Natural History, Smithsonian Institution, Washington, D.C. 20560-0119, USA
[5]Los Alamos National Laboratory, NIS-2, MS-D436, Los Alamos, New Mexico 87545, USA
[6]Smithsonian Astrophysical Observatory, 60 Garden Street, MS-4, Cambridge, Massachusetts 02138, USA
[7]University of Arizona, Department of Planetary Science, Space Sciences Building, Tucson, Arizona 85721, USA
[8]Southwest Research Institute, Space Science and Engineering, 6220 Culebra Road, San Antonio, Texas 78228-0510, USA
[†]Present Address: Carnegie Institution of Washington, Department of Terrestrial Magnetism, 5241 Broad Branch Road Northwest, Washington D.C., 20015, USA
[‡]Present Address: St. Joseph's College, West Hartford, Connecticut 06117-2791, USA
*Correspondence author's e-mail address: lrn@dtm.ciw.edu

(Received 2001 August 3; accepted in revised form 2001 October 9)
(Part of a series of papers on the Near–Shoemaker mission to 433 Eros)

Abstract–We report major element ratios determined for the S-class asteroid 433 Eros using remote-sensing x-ray fluorescence spectroscopy with the near-Earth asteroid rendezvous Shoemaker x-ray spectrometer (XRS). Data analysis techniques and systematic errors are described in detail. Data acquired during five solar flares and during two extended "quiet Sun" periods are presented; these results sample a representative portion of the asteroid's surface. Although systematic uncertainties are potentially large, the most internally consistent and plausible interpretation of the data is that Eros has primitive Mg/Si, Al/Si, Ca/Si and Fe/Si ratios, closely similar to H or R chondrites. Global differentiation of the asteroid is ruled out. The S/Si ratio is much lower than that of chondrites, probably reflecting impact-induced volatilization and/or photo- or ion-induced sputtering of sulfur at the surface of the asteroid. An alternative explanation for the low S/Si ratio is that it reflects a limited degree of melting with loss of an FeS-rich partial melt. Size-sorting processes could lead to segregation of Fe-Ni metal from silicates within the regolith of Eros; this could indicate that the Fe/Si ratios determined by the x-ray spectrometer are not representative of the bulk Eros composition.

INTRODUCTION

The relationship between asteroids and meteorites is a crucial problem in planetary science. Meteorites provide us with detailed information about a wide array of processes in the early solar system (Kerridge and Matthews, 1988). Many of the same processes seem to be reflected in the spectral data obtained for specific groups of asteroids by astronomical observations. The data obtained from both meteorites and asteroids provide powerful constraints on models of the solar nebula, planet formation and geological processing on planetary bodies. However, taking full advantage of the complementary data sets provided by asteroid and meteorite studies requires knowledge of the location within the solar system of the parent bodies of specific meteorite classes.

Previous studies linking asteroids to meteorite classes have been primarily based either on dynamical calculations or on telescopic observations of spectral reflectance in the visible and near-infrared portions of the electromagnetic spectrum (*e.g.*, Wetherill, 1985; Gaffey *et al.*, 1993a). Important data have also been obtained by flybys of a few asteroids, including Gaspra and Ida, visited by the *Galileo* spacecraft in 1993. A new era in asteroid-meteorite studies has opened with NASA's near-Earth asteroid rendezvous (NEAR)–Shoemaker mission (Cheng, 1997). The *NEAR–Shoemaker* spacecraft successfully ended its mission to the asteroid 433 Eros by landing on the body on 2001 February 12. In its 1 year long orbital mission, NEAR returned to Earth a huge body of data from six scientific experiments, including a multi-spectral imager (MSI), a near-infrared spectrometer (NIS), a magnetometer, a laser

Prelude preprint MS#4615

rangefinder, an x-ray spectrometer (XRS) and a gamma-ray spectrometer (GRS). These instruments allow much more detailed exploration of the properties of a specific asteroid than obtained by astronomical observation and provide complementary information for clarifying the relationship between asteroids and meteorites. In particular, the x-ray and gamma-ray spectrometers have allowed for the first time the surface elemental composition of an asteroid to be directly measured.

Eros, discovered in 1898, is termed a near-Earth asteroid because its orbit crosses that of Mars, in contrast to the main-belt asteroids whose orbits lie between those of Mars and Jupiter. It is classified as an S asteroid (S(IV) in the scheme of Gaffey *et al.*, 1993b). S asteroids are the second most abundant asteroid class and the most abundant in the inner asteroid belt. Reflectance spectra indicate that their surfaces contain the mafic silicates olivine and pyroxene as well as a "reddening" agent, commonly assumed to be Fe-Ni metal. A critical question is whether S asteroids are the source bodies of ordinary chondrites, which dominate the flux of meteorites delivered to the Earth. Dynamical calculations have suggested such a link (Wetherill, 1985), but spectral differences between the asteroids and laboratory measurements of ordinary chondrites have complicated the issue. The surfaces of airless planets interact with micrometeorites, solar photons and solar and galactic charged particles. The consequent changes in optical properties of surface materials have been termed "space weathering" and many researchers have postulated that such processes are responsible for the spectral differences between S asteroids and ordinary chondrites (*e.g.*, Pieters *et al.*, 2000 and references therein). Space weathering of lunar soils manifests itself by the formation of agglutinate glasses by micrometeorite impacts and the formation of vapor-deposited nanophase metallic iron grains on the surfaces of soil particles. It is not yet known to what extent these processes should affect asteroids. Chapman (1996) argued that *Galileo* observations of Gaspra and Ida provided evidence for asteroidal space weathering. More recently, Pieters *et al.* (2000) showed that models of production of nanophase iron in ordinary chondrite regoliths could explain well the spectral differences between S asteroids and ordinary chondrites measured in the laboratory.

This paper reports elemental abundance ratios determined for the surface of Eros by remote-sensing x-ray fluorescence spectroscopy using the NEAR XRS. In this technique, x-rays emitted from the solar corona interact with the asteroid's surface producing characteristic fluorescent emission from the atoms present. The fluorescent x-rays are detected by the orbiting detector, together with solar x-rays scattered from the surface. The most prominent characteristic x-ray fluorescent lines that can be observed by the NEAR XRS are the Kα lines from the major elements Mg (1.254 keV), Al (1.487 keV), Si (1.740 keV), S (2.308 keV), Ca (3.691 keV), and Fe (6.403 keV). The sampling depth is <100 μm for these elements. Trombka *et al.* (2000) reported preliminary compositional results from NEAR XRS data obtained during the first few months of the orbital mission. Since that initial report we have obtained additional data and refined our analysis techniques and x-ray fluorescence models. These are described herein.

NEAR-SHOEMAKER X-RAY SPECTROMETER

The NEAR–Shoemaker XRS has been described in great detail elsewhere (Goldsten *et al.*, 1997; Trombka *et al.*, 1997; Starr *et al.*, 2000) so we describe it only briefly. The asteroid-pointing detector package consists of three sealed gas-filled proportional counters, each with 25 cm^2 collecting area and thin (25 μm) Be windows. A honeycomb-shaped collimator made of Cu and 3% Be limits the full field of view of the detectors to ~5° to improve spatial resolution and reduce cosmic x-ray background. This gives an optimal spatial resolution of ~3 km at a distance of 40 km from the asteroid's surface.

The fractional energy resolution of the proportional counter detectors varies inversely with the square root of energy and is ~14% at 5.9 keV. The energy resolution is not sufficient to resolve the characteristic Kα lines of Mg, Al and Si (at 1.254, 1.487 and 1.740 keV, respectively), and a balanced filter system, similar to that used on the Apollo 15 and 16 missions (Adler *et al.*, 1972a–c), is used to resolve these geochemically important lines. Two of the detectors have ~9 μm thick absorption filters mounted externally. A Mg filter on one detector effectively attenuates the Al and Si lines, and an Al filter on another blocks the Si line. The third detector is unfiltered and allows all three lines to pass, attenuated only by the Be window. By analyzing the three detector spectra simultaneously, the flux of photons in the three lines can be uniquely determined.

The balanced filter system has an unintended negative effect. The strong absorption of x-rays by the filters can lead to fluorescence of the filters themselves, adding an unwanted background signal. For Mg, where the signal from the asteroid is strong, this is a negligible effect. Similarly, because the lunar surface is rich in Al, this was probably a negligible effect for XRS Al measurements from the Apollo missions (Adler *et al.*, 1972a–c). However, it was clear from the earliest NEAR flare spectra from Eros that the asteroid has a low Al abundance (Trombka *et al.*, 2000), and we have to address the possibility that some of the Al signal in the Al-filtered detector is from the filter. Modeling of this effect, assuming an ordinary chondrite composition for Eros and typical solar flare spectra, indicates that some 10–20% of the Al *fluorescence* signal measured in the Al-filtered detector indeed is from the filter. However, as described below, because of the low Al abundance, the total Al signal measured in the NEAR XRS is in fact dominated by scattered solar photons, not by fluorescence x-rays. The effect of the filter "enhancement" on the total Al signal in the Al-filtered detector is predicted to be 5–10%. For completeness, we have included this effect in our theoretical models used to convert photon spectra to elemental abundances. However, its magnitude is smaller than our uncertainty due to other effects.

As discussed below, conversion of photon spectra to elemental abundances requires knowledge of the solar x-ray spectrum. To this end, two x-ray detectors, a Si PIN photodiode and a gas-filled proportional counter, were mounted on the forward deck of the *NEAR–Shoemaker* spacecraft and monitored the solar flux. The PIN detector was flown as an engineering test and was not used during the orbital encounter with Eros. The proportional counter is identical to the asteroid-pointing detectors but has a graded shield specially designed to restrict the effective area of the detector to ~1 mm^2 and to block most of the low-energy (<3 keV) solar flux to enhance the detector response at higher energy (Clark *et al.*, 1995). Unfortunately, the response of this shield as a function of energy and solar incidence angle was not measured in the laboratory prior to flight due to schedule constraints and must be calculated from assumed properties of the filter materials. This is discussed in more detail below.

The primary source of background in the XRS detectors is interactions of galactic and solar cosmic rays with the gas. To reduce this unwanted background, rise-time discrimination circuitry was used. The rejection efficiency for charged particles and gamma rays was determined to be ~70% at 5.9 keV (Starr *et al.*, 2000). Rise-time discrimination was not used below 3 keV because below this energy the difference in rise time between x-rays and cosmic rays is not sufficient to reject the background without also greatly diminishing the number of valid x-ray events. The absolute count rate of the background was found to vary by several percent on a timescale of days to weeks. Variations in spectral shape are smaller but significant for the lowest signal-to-noise spectra. In addition, there were occasional periods of intense solar-particle activity during the orbital encounter with Eros, most notably during mid-July 2000, when many flares and coronal mass ejections occurred in a relatively short span of time. During these periods variations in background shape and intensity occurred on a shorter time scale of tens of minutes to hours, making accurate background subtraction of asteroid-pointing spectra difficult. As a result, we do not consider data from these time periods here.

DATA SELECTION AND ANALYSIS TECHNIQUES

Data Selection

The solar x-ray flux and hence fluorescent flux from the asteroid increases greatly during flares, allowing statistically significant results to be obtained in a relatively short period of time. During non-flaring times ("quiet Sun"), the fluorescent flux is much lower, and many more spectra must be co-added to obtain significant results. During the periods of 2000 May to August and 2000 December to 2001 February, the *NEAR–Shoemaker* spacecraft was in 50 and 35 km orbits around the center-of-mass of Eros. It was in these time periods that significant XRS data were acquired; the signal-to-noise ratio was too low when in higher orbits. During these orbits, the Sun was near the maximum of its 11 year activity cycle, and more than 100 solar flares occurred. Unfortunately, the combination of requirements that the NEAR solar panels always face the Sun, the highly non-spherical shape of Eros and the ~8 h/day spent telemetering data to Earth led to observable fluorescence from the asteroid for only a fraction of the flares that occurred. In addition, many of the observed flares occurred in highly unfavorable viewing geometries, especially high solar incidence and/or asteroid emission angles. The signal-to-noise ratio decreases, and the x-ray fluorescence and scatter models that we use to reduce the data are less reliable under these conditions.

Here we report data acquired during five solar flares and longer spectral sums for two quiet Sun periods (Table 1). The quiet Sun spectra were divided into those collected during the May through August 2000 ("summer") and during December 2000 through February 2001 ("winter"); only spectra with incidence and emission angles <60° were included in the sums. The flares were chosen as those with relatively high signal-to-noise ratios and incidence and emission angles <60°. The large flare that occurred on 2000 July 19, and was discussed in our preliminary report (Trombka *et al.*, 2000) is not included here for two reasons. First, this flare occurred during a period of intense solar activity and the background shape and intensity changed rapidly during the day, precluding accurate background

TABLE 1. Basic data for analyzed solar flares and quiet Sun integrations.

Spectrum	UT	Total integration time (s)	Latitude (°)	Longitude (°)	Average GOES temperature (MK)
2000 May 4 Flare	4:40	950	17	146	14.5
2000 June 15 Flare	19:49	2250	–22	153	11.9
2000 July 10 Flare	22:00	3750	6	266	10.6
2000 December 27 Flare	15:40	1000	–5	175	14.2
2001 January 2 Flare	7:52	1700	–27	106	12.7
Quiet Sun, 2000 May 2 to August 27	–	402800	–	–	4.23 ± 0.4
Quiet Sun, 2000 December 12 to 2001 February 10	–	357500	–	–	3.89 ± 0.4

subtraction for the flare spectra. Second, the NEAR solar monitor was not operating correctly during this flare, due to a major solar particle event shortly before the flare. As a result, we do not have a measurement of the solar spectrum needed to convert the observed photon fluxes to elemental abundances.

The regions of Eros observed by NEAR during the solar flares and quiet Sun measurements, called footprints, are shown in Fig. 1. All of the five flare footprints lie between ±45° latitude. Four flare footprints overlap to varying extent and are concentrated in the western hemisphere of Eros. Two of these, those from May 4 and June 15, overlap the 5.5 km crater known as Psyche. The footprint from 2000 December 27 lies mainly on the western end of the asteroid. The footprint from 2000 July 10 samples the edge of the large saddle-shaped depression known as Himeros. Although the flare coverage is far from uniform, the flares do sample a significant fraction of the asteroid's surface. The summer quiet Sun spectra are concentrated around Psyche and Himeros. The coverage of the winter quiet Sun spectra, on the other hand, is quite different; these spectra are entirely from the southern hemisphere and some of the highest coverage is from areas not well-sampled during the summer.

During the low-orbit mapping phase, XRS spectra were acquired every 50 s. For all but the July 10 flare, which did not exhibit Fe fluorescence, we only included spectra with obvious counts in the 6.4 keV Fe line. In addition, for all five flares we only included those spectra acquired after the solar x-ray flux reached its maximum, during the decay phase. Spacecraft observations have indicated that the solar x-ray emitting plasma is strongly multi-thermal during the initial stages of a flare and becomes more isothermal during the decay phase (Garcia, 1994). Our modeling of Eros x-ray spectra largely depends on the assumption of an isothermal plasma, so only including spectra collected during the decay phase should reduce systematic uncertainties due to this simplification.

The pulse-height spectra from the four NEAR XRS detectors are shown in Fig. 2 for the five solar flares. The three asteroid-pointing spectra for the two quiet Sun spectral sums are shown in Fig. 3. The spectra have been background-subtracted and error bars indicate Poisson statistics in each channel. Plotted curves are fits to the spectra as described in the following sections.

Background Subtraction and Spectral Deconvolution

In addition to fluorescent x-rays from the surface of Eros, NEAR asteroid-pointing x-ray spectra also include a cosmic-ray induced background and scattered solar x-rays. For the solar flare spectra, the background was taken to be the sum of all spectra acquired during the same day as the flare during periods when the field-of-view of the detector did not include any solar-illuminated asteroid (dark-side or off-pointing spectra). For the quiet Sun spectra, the background was the sum of all off-pointing spectra acquired over the same time period as the summed fluorescence spectrum. A separate background was determined for each of the three asteroid-pointing detectors, normalized to the fluorescence spectra and subtracted. For the flares, the background was simply normalized according to integration time, reflecting the fact that the background changed slowly on the timescale of one day. For the longer quiet Sun spectra, the magnitude of the background was adjusted as part of the spectral fitting routine.

Once spectra were background subtracted, they were deconvolved to determine photon fluxes of Mg, Al, Si, S, Ca and Fe K x-rays. The three asteroid-pointing detector spectra were fitted simultaneously using a Levenberg–Marquardt least-squares minimization routine (Marquardt, 1963). For most spectra, the fitting function was a sum of seven Gaussian lines for each detector (Kα for all elements, also Kβ for Fe) with the relative amplitudes of each determined by the relative detector efficiencies. For the quiet Sun and July 10 flare, S (only quiet Sun), Ca and Fe were excluded from the fit since these are absent from the spectra. The free parameters in the fits were the number of photons of each element incident on the detectors and the energy calibration parameters (gain and zero) in each detector. For the flare spectra, the width of the Gaussian lines was fixed according to the measured energy resolution of the detectors. For the quiet Sun spectra, the energy resolution was slightly degraded relative to the measured resolution. This was to compensate for peak broadening due to gradual gain changes during the long periods over which the spectra were acquired. Also, the magnitude of the background in each detector was allowed to vary during the quiet Sun fits. From the fit results, we derived photon flux ratios relative to Si. The derived uncertainties for the photon ratios include the effect of correlated errors between fitting parameters. The results of these fits are overlain on the NEAR spectra in Fig. 2.

The uncertainties in the photon fluxes and flux ratios determined by the fit are based largely on counting statistics but also take into account the goodness-of-fit as determined by the reduced χ^2. Strictly speaking, this is mathematically unjustified because the fitting function is not an exact model of the observed spectra. In addition to the Gaussian lines from the major elements, the spectra include a scattered solar continuum and signals from other elements, including Ti, Mn and Cr. These are predicted to be small relative to the major lines, but even so, the best fit would result in a reduced $\chi^2 > 1$. However, in order to convert observed photon ratios to elemental abundance ratios, as discussed below, we generate theoretical NEAR spectra and fit them using the same fitting routines. Thus, the same fitting function is applied to the observed and theoretical spectra, and we can have some confidence in the results. To estimate the "true" errors in the spectral fitting, we have generated theoretical spectra for several assumed asteroid compositions and a range of assumed incident solar spectra. For each composition/solar spectrum, we calculated 50 models in which we scaled theoretical spectra to typical observed intensities, added statistical noise and performed the spectral deconvolution. The standard deviations of the resulting derived photon flux ratios were taken as a

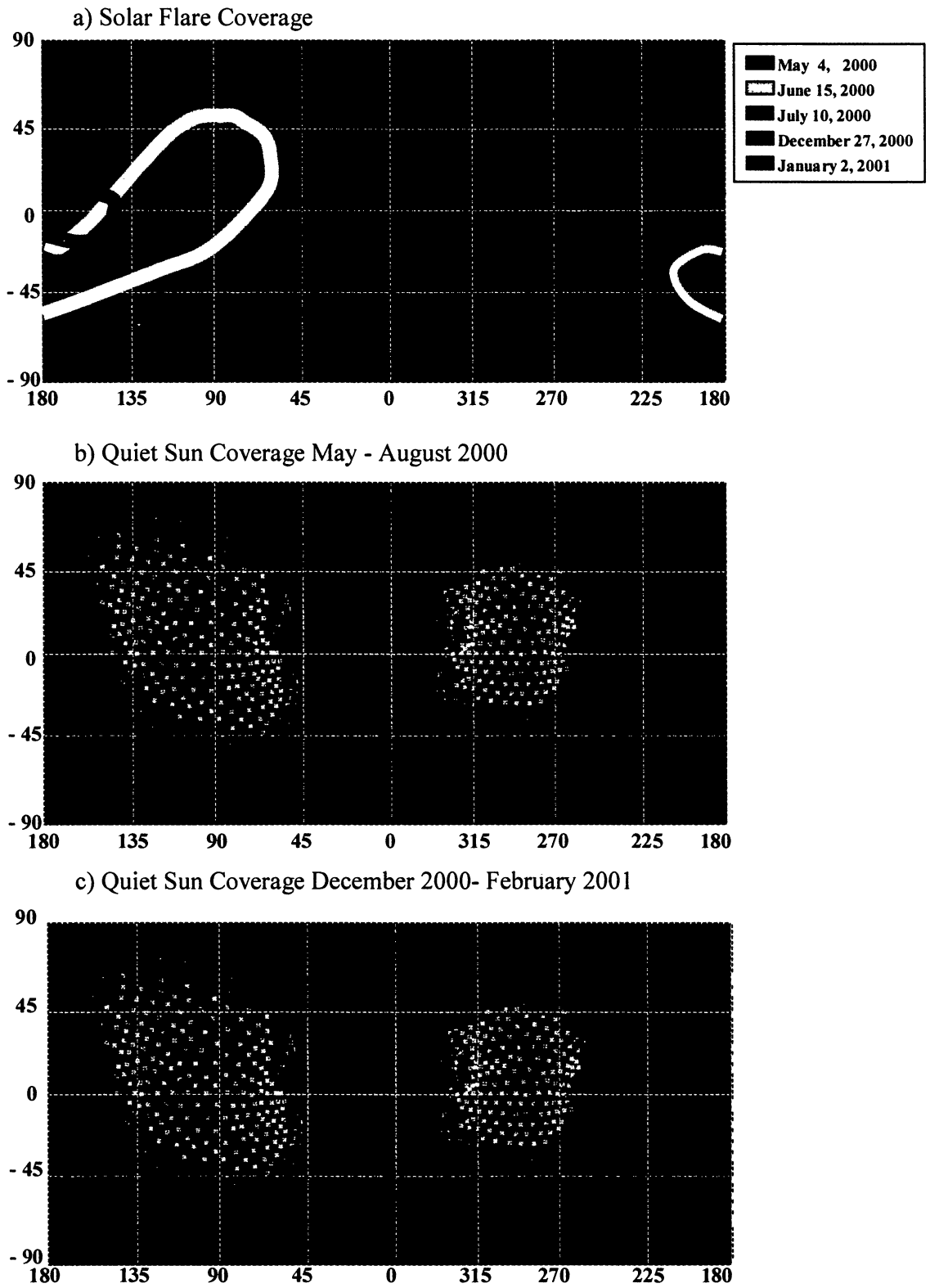

FIG. 1. XRS coverage of Eros, overlaid on a mosaic of NEAR MSI images, projected onto an evenly spaced latitude-longitude grid. The 5.5 km crater, Psyche, is at upper left; the saddle-shaped depression, Himeros, is at mid-right. Footprints from five solar flares are shown in (a). Coverage during long "quiet Sun" (non-flaring) x-ray spectral sums is shown in (b) for the period of 2000 May 4 to 2000 August 27, and in (c) for 2000 December 12 to 2001 February 12. In (b) and (c), colored points indicate vertices of a plate model of the asteroid's shape, color-coded to indicate total x-ray accumulation time for the associated plate. Coverage increases in order: dark blue, light blue, green, red, yellow.

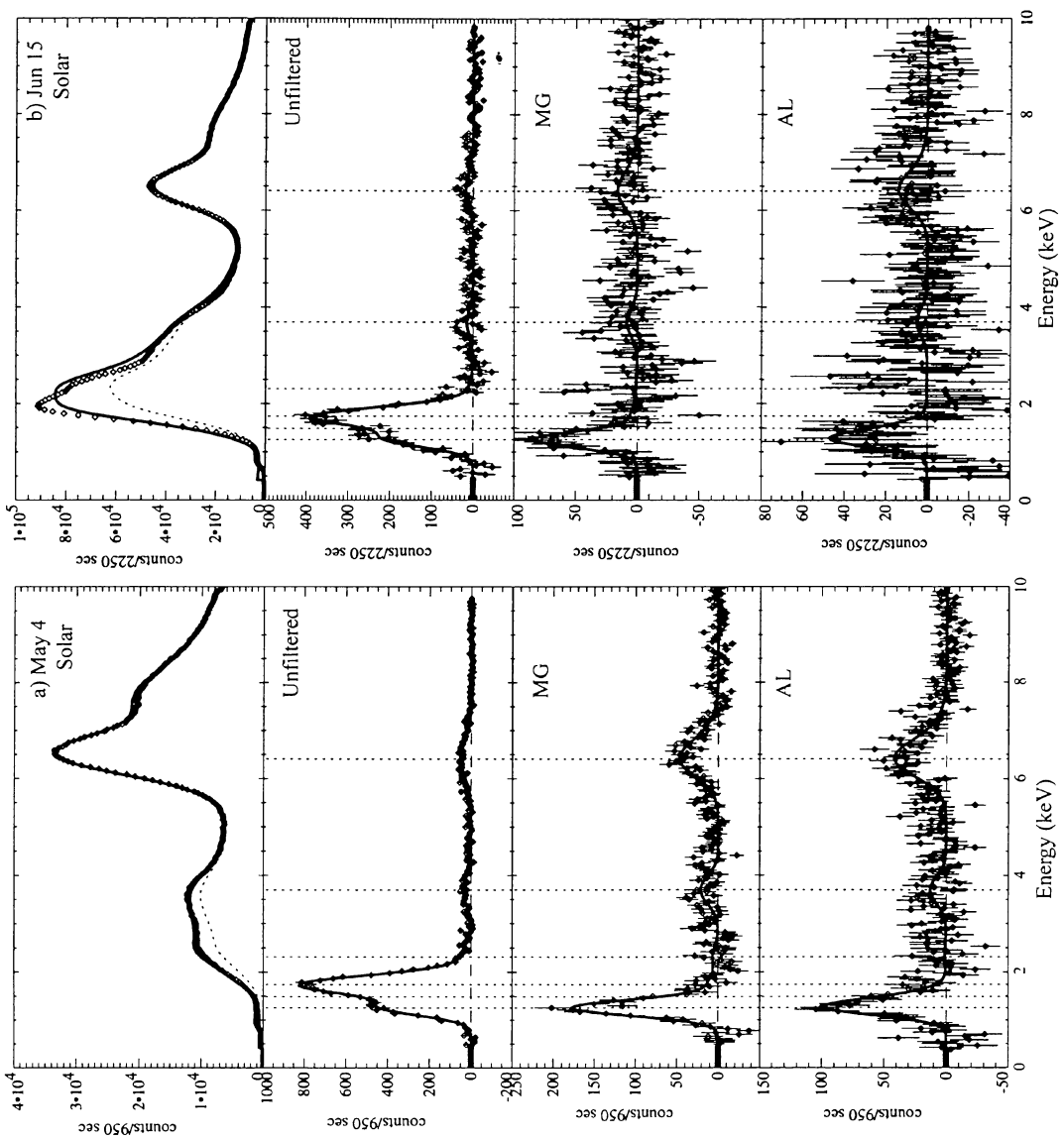

FIG. 2. NEAR XRS spectra observed during five solar flares. Top-to-bottom for each event: solar monitor spectrum, unfiltered asteroid-pointing spectrum, magnesium-filtered asteroid-pointing spectrum, and aluminum-filtered asteroid-pointing spectrum. Solid curves on solar monitor spectra are fits assuming two solar plasma temperatures (F1); dashed curves indicate single-temperature fits to >4 keV portion of spectra (F2). Asteroid-pointing spectra are background-subtracted; 1σ error bars are due to counting statistics. Solid curves are spectral fits. Vertical dashed lines indicate positions of Kα x-ray lines for (left-to-right) Mg, Al, Si, S, Ca and Fe. (a) 2000 May 4; (b) 2000 June 15.

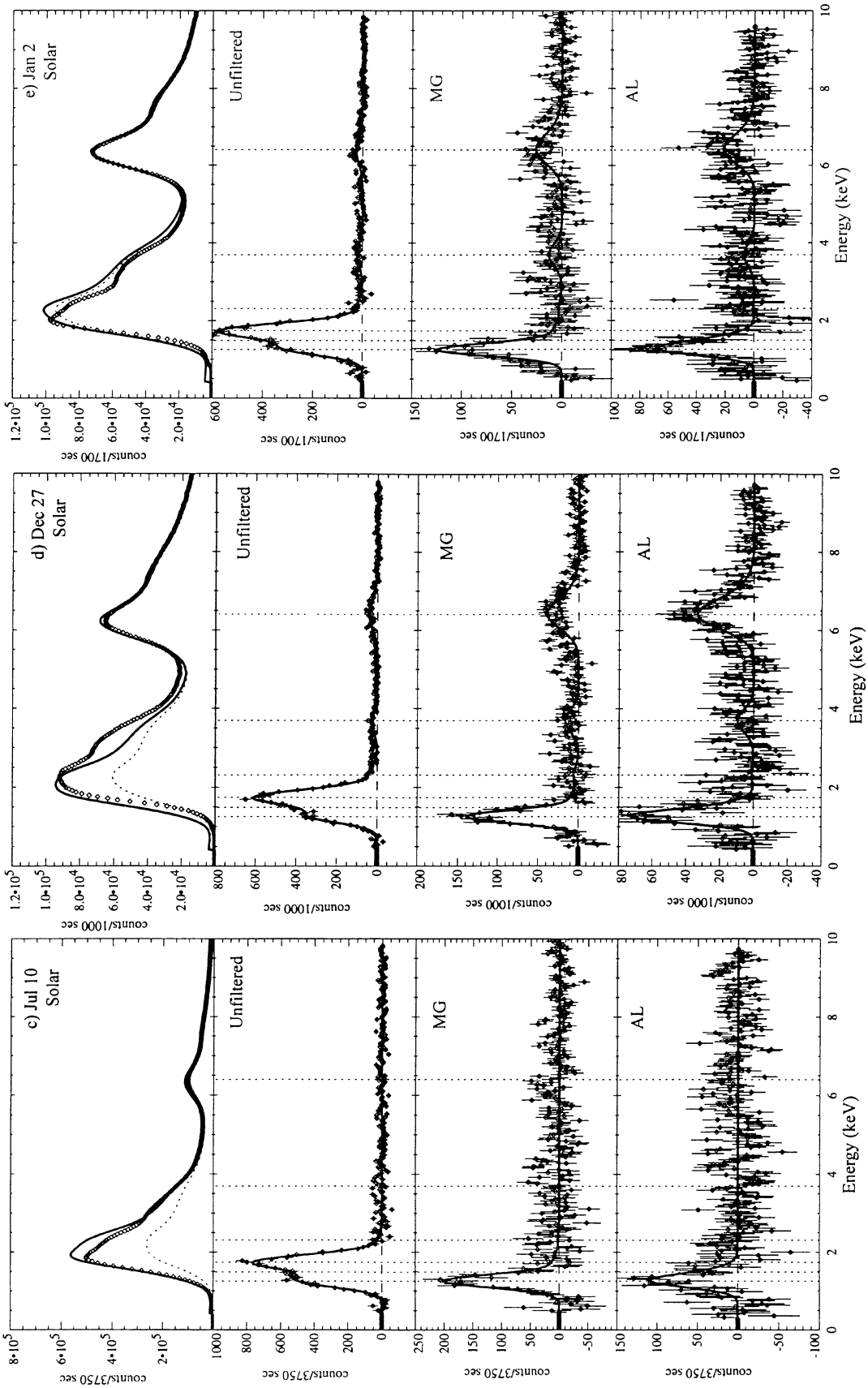

FIG. 2. *Continued.* NEAR XRS spectra observed during five solar flares. (c) 2000 July 10; (d) 2000 December 27. (e) 2001 January 2.

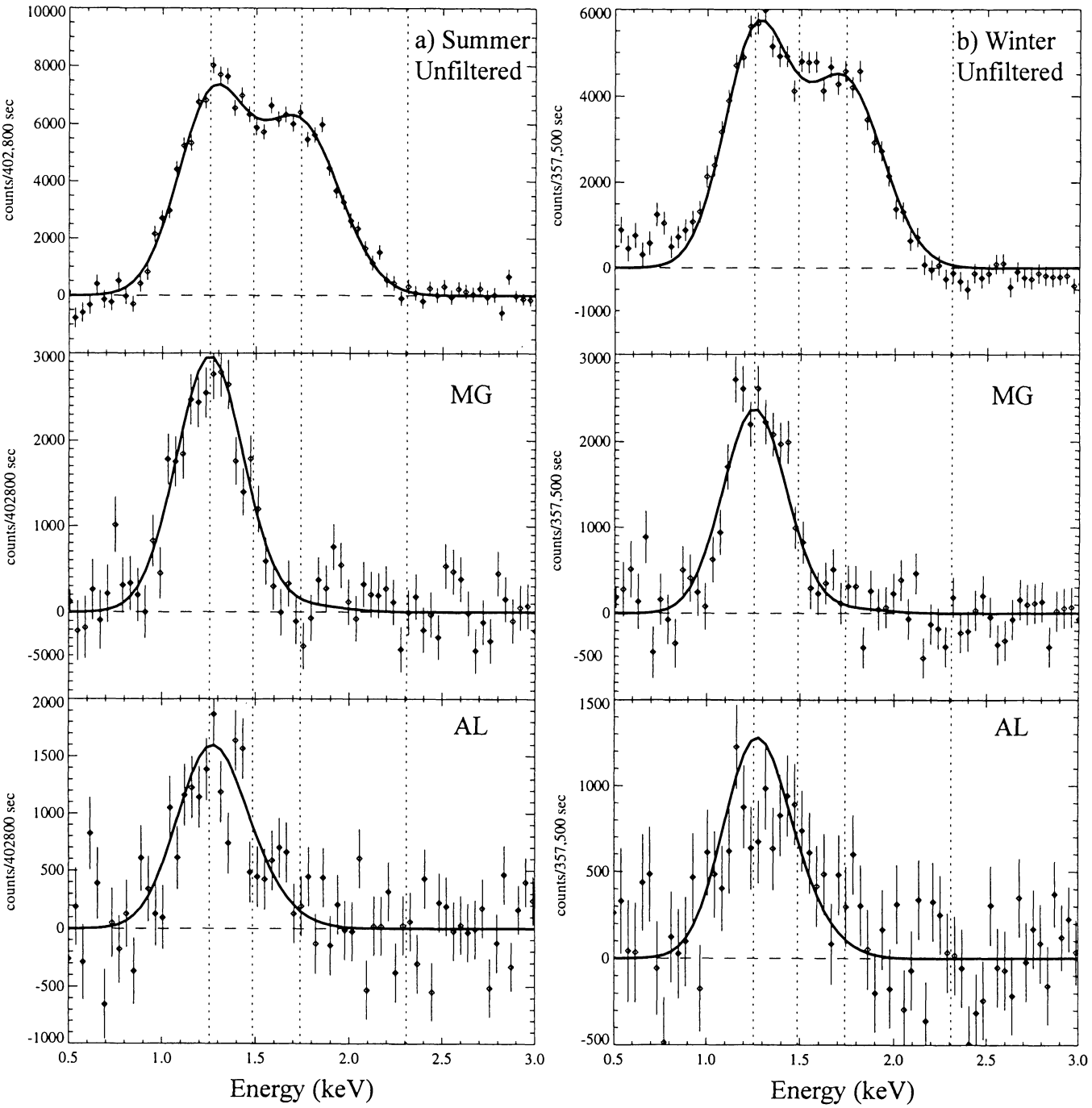

FIG. 3. Background-subtracted NEAR asteroid-pointing XRS spectra, acquired during periods of quiet Sun (non-flaring conditions). One sigma error bars are due to counting statistics; solid curves are fits to spectra. Vertical dashed lines indicate positions of Kα x-ray lines for (left-to-right) Mg, Al, Si, and S. (a) Spectral sum from 2000 May 2 to 2000 August 27; (b) spectral sum from 2000 December 12 to 2001 Februrary 10.

measure of the actual uncertainties; these were in almost all cases smaller than the uncertainties derived directly from the fitting results. Thus, we believe that reporting uncertainties as derived by the fitting routine is a conservative approach. In any case, the error budget for our derived abundances of Eros is dominated by systematic errors.

Solar Spectra

Incident solar x-rays provide the excitation source for x-ray generation from the surface of Eros. Converting observed photon fluxes from Eros to elemental abundances thus requires accurate knowledge of the incident solar x-ray spectrum. The

solar flux from 1 to 10 keV is composed of a multitude of lines from highly ionized atoms superimposed on a continuum. The spectrum of isothermal solar plasma has been modeled as a function of temperature (*e.g.*, Mewe *et al.*, 1985; Raymond and Smith, 1977). Here, we use the theoretical solar spectra of Mewe *et al.* for our analyses. Theoretical spectra for three temperatures, 4, 8 and 16 × 10^6 K (MK), are shown in Fig. 4. Solar x-ray intensity decreases by several orders of magnitude from 1 to 10 keV, so fluorescent lines and scattered radiation exhibit greater intensity at lower energies. As the solar temperature increases, usually in conjunction with flares, the spectrum hardens, with increased output at higher energies, reduced steepness in the spectral slope, and increased overall x-ray flux. This hardening of the solar spectrum is reflected in the observed NEAR spectra (Figs. 2 and 3): the spectra acquired during high-temperature solar flares exhibit Ca and Fe fluorescence, while the quiet Sun spectra only show Mg, Al and Si. Moreover, the observed photon ratio of Mg to Si decreases with increasing solar temperature as the spectral hardening induces higher relative fluorescence of Si.

In our preliminary XRS report (Trombka *et al.*, 2000), solar temperatures for the analyzed NEAR spectra were determined using broad-band x-ray flux measurements from the geostationary operational environmental satellite 8 (GOES), which was observing much of the same portion of the Sun as NEAR was during the summer of 2000. GOES measures the solar x-ray flux in two wavelength bands (corresponding to about 1.6–12 keV and about 3–25 keV) every 3 s. Techniques to calculate solar temperature from GOES data have been published by Thomas *et al.* (1985) and Garcia (1994). These models assume that the x-ray emitting solar plasma is isothermal and the estimated uncertainty in derived temperature is 10–20%. This uncertainty is too large to permit accurate determination of Fe and Ca abundances from NEAR XRS spectra, assuming GOES temperatures. Moreover, high-spectral-resolution observations of x-ray lines of Ca and Fe by the bragg crystal spectrometer on the *Yohkoh* spacecraft indicate that flares often include higher temperature components than the average temperature determined by GOES (Feldman *et al.*, 1996). These results indicate that GOES temperatures are not sufficiently accurate to quantitatively determine abundances from NEAR XRS spectra, and we hence depend on the NEAR solar monitor itself to infer solar spectra.

The graded shield on the NEAR solar monitor (Clark *et al.*, 1995) provides the high dynamic range needed to measure the solar spectrum for a wide range of temperatures. To do so, it attenuates several orders of magnitude of the solar signal below 5 keV and essentially all of the flux below ~2 keV. Under these conditions, uncertainties in the physical properties of the graded shield translate into large uncertainties in incident solar spectra inferred from observed spectra. Because the efficiency of the solar monitor as a function of energy and solar incidence angle was not measured prior to flight, we must calculate the response function from the assumed properties of the graded

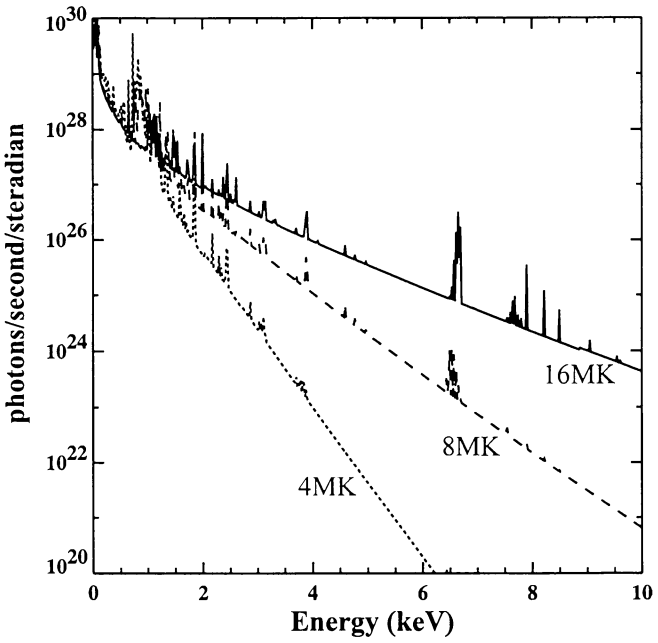

FIG. 4. Theoretical solar x-ray spectra for three plasma electron temperatures, calculated using the model of Mewe *et al.* (1985). The solar x-ray spectrum is composed of lines from highly-excited ions, superimposed on a continuum. As the plasma temperature increases, the spectrum "hardens", with increased output at higher energies.

shield. Unfortunately, there are a large number of uncertain parameters that affect this calculation. Most of the low-energy solar flux is attenuated by layers of Al, Be, and the plastics delrin and kapton. The calculated x-ray attenuation coefficients for these materials depend on their composition, density and thickness. The composition and density of the plastics are only known approximately and may change due to exposure to outer space. Moreover, most of the signal that is observed passes unimpeded through pinholes in the filter layers of the graded shield. The exact size of these holes is known to a few percent based on engineering tolerances and again may have changed due to temperature-dependent expansion or contraction of the plastics in space. Finally, for spectra obtained at high incidence angle, the exact physical dimensions of the entire shield must be known for accurate determination of the response function.

We have calculated solar monitor response functions for different sets of parameters (pinhole size, delrin density, *etc.*). To determine the best set of parameters we have generated synthetic spectra for a range of solar temperatures and incidence angles by convolving theoretical spectra of Mewe *et al.* (1985) with various calculated response functions. The resulting model spectra were compared with observed solar spectra. Based on this study, we have chosen a preferred response function to use in fitting solar monitor spectra. Below ~4 keV, this response function is still uncertain and while some NEAR spectra can be matched well, others are less satisfactory. Above this energy, the response function is much more certain, and we generally

can match this portion of the spectra well with synthetic spectra. Some of the remaining discrepancy in spectral shape between models and observations at low energy may be due to errors in the Mewe *et al.* spectra, due to variations in coronal elemental abundances for example. In any case, continued studies are needed to pin down the exact response function of the solar monitor, for instance examination of spectra obtained early in the mission when the PIN solar monitor detector was in use along with the proportional counter.

We have used our preferred response function to infer incident solar spectra for the flares reported here. Because the solar temperature can change rapidly during flares we analyzed individual 50 s integrations of the solar monitor. For each spectrum we performed two fits. In the first, we only fit the high-energy (>5 keV) portion of the spectrum. The response function is more certain there, and if the flare is multi-thermal this fit should sample the higher temperature component. Synthetic spectra were generated for a range of temperatures and the appropriate solar incidence angle, and the one that matched the observed spectrum best (in a least-squares sense) was selected. Free parameters in the fit were the overall normalization, which is related to the emission measure or plasma density, and the zero point of the detector calibration. The latter can shift during a flare because of the lack of baseline restoration in the readout electronics of the solar monitor (Goldsten *et al.*, 1997). In the second fit, the best high-energy fit was subtracted from the observed spectrum and a lower temperature spectrum was fitted to the residual spectrum. The results of these fits are plotted on the solar monitor spectra in Fig. 2. In all cases the fit at high energy is much better than at low energy, probably reflecting residual errors in the response function and/or the theoretical solar spectra.

We did not fit the solar monitor data for the quiet Sun spectra, both because it was impractical to perform the fits for the more than 15 000 individual integrations included and because of the remaining uncertainties in the low-energy part of the response function. For the analysis of these spectra, we thus rely on the average GOES temperature assuming a 10% uncertainty in the derived temperatures at ~4 MK (Garcia, 1994).

X-Ray Models

In laboratory x-ray fluorescence measurements, quantitative analysis is accomplished *via* the use of standards. This luxury is not available in planetary remote-sensing, and we must use models to convert photon spectra to elemental abundances. Our basic approach involves a number of steps. We use standard analytical models of primary x-ray fluorescence (*e.g.*, Jenkins and DeVries, 1969; Clark and Trombka, 1997) and coherent scatter (Hubbell *et al.*, 1969). Incoherent scatter and secondary and higher levels of fluorescence are expected to be negligible. X-ray absorption coefficients are taken from Hubbell and Seltzer (1997). Atomic structure factors, needed for the coherent scatter calculation, are taken from Hubbell *et al.* (1975). Fluorescence yields are from Krause (1979). The fluorescence intensity of a given x-ray line depends not only on the concentration of the corresponding element but also on the concentration of all other elements in the sample. In addition, the geometry of the observation is important, namely the solar incidence angle on the surface of Eros and the emission (viewing) angle that the boresite of the XRS detector makes with the surface normal. The coherently scattered intensity depends on the angle between the incoming solar photon and the boresite vector. All of these angles are computed for each XRS integration from spacecraft pointing data and a shape model for the asteroid (McClanahan *et al.,* 1999). The validity of the basic x-ray fluorescence and scatter models has been confirmed previously by the analysis of lunar x-ray spectra from Apollo 15 and 16 (Adler *et al.*, 1972a–c; Clark, 1979; Clark and Trombka, 1997), although additional laboratory validation is desirable.

For a given solar spectrum, assumed composition and viewing geometry, the models can be used to calculate theoretical x-ray spectra from Eros. Example spectra for an LL-chondrite composition and two solar temperatures are shown in Fig. 5a. The same spectra, convolved through the efficiency of the NEAR unfiltered detector, are shown in Fig. 5b,c. In Fig. 5b,c, the coherently scattered contributions to the total spectra are also plotted. For the major elements Mg, Si and Fe, the corresponding x-ray emission lines are dominated by fluorescence from the asteroid. For the less abundant elements Al, S, and Ca, scattered solar photons have comparable intensity to the fluorescent photons. Thus, our inferred Al, S, and Ca abundances are somewhat dependent on the assumed scatter model.

As in Trombka *et al.* (2000), here we consider elemental ratios rather than absolute abundances. This is because ratioing eliminates some of the geometrical factors affecting the production and scatter of x-rays. We ratio abundances to Si, because it fluoresces under quiet Sun and solar flare conditions and because its x-ray line lies between the two other most abundant observable rock-forming elements, Mg and Fe. As shown in Trombka *et al.* (2000), these ratios are very good discriminants of many meteorite classes and geological processes. We also consider the Fe/Ca ratio for reasons made clear below.

A set of calibration curves relating photon ratios to elemental abundance ratio was calculated for the observational geometry and solar spectrum of each flare and the quiet Sun integrations. For the flares, the assumed solar spectra were the weighted sums of theoretical spectra corresponding to the individual temperatures fitted to the solar monitor for each 50 s integration; a single temperature spectrum corresponding to the average GOES temperature was used for the quiet Sun integration. To generate calibration curves for a given solar spectrum and observational orientation, we calculated model fluorescence and coherent scatter spectra for 22 measured meteorite compositions, corresponding to a wide range of meteorite types.

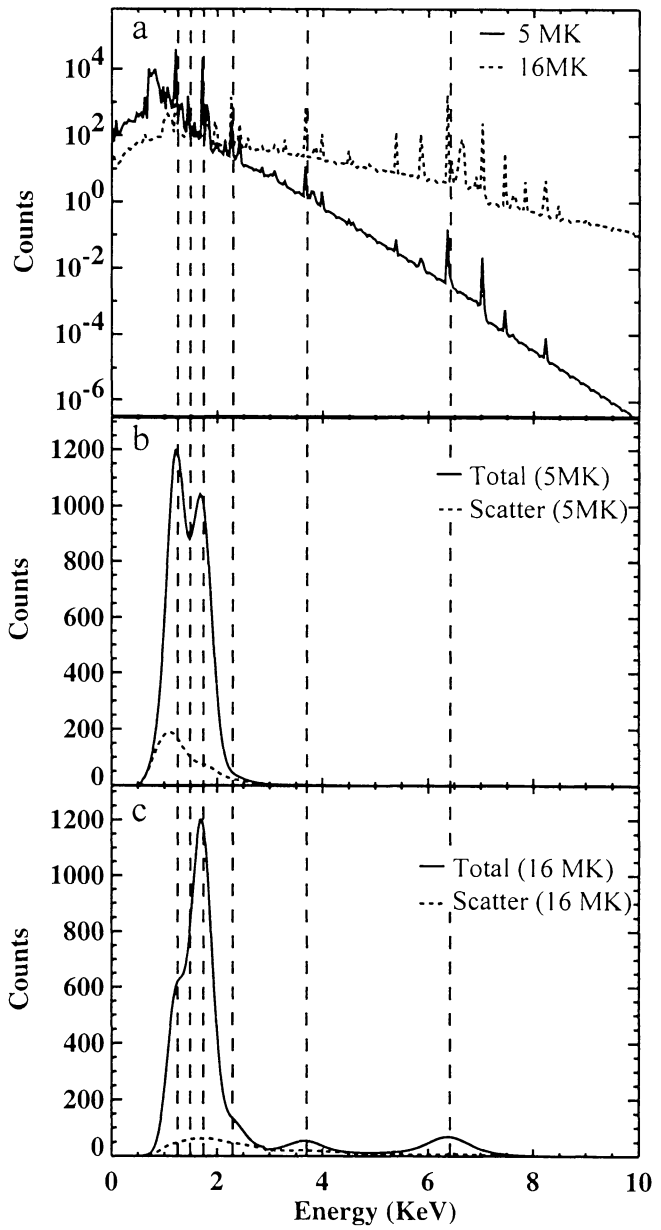

FIG. 5. Theoretical x-ray (fluorescence and coherent scatter) predicted for an LL-type ordinary chondrite composition and incident x-ray spectra corresponding to two solar plasma temperatures: 5 and 16 MK. (a) High-resolution photon spectra; (b) 5 MK photon spectrum convolved with NEAR unfiltered detector response function; solid curve is total x-ray spectrum, dashed curve is coherently-scattered portion of spectrum. (c) 16 MK photon spectrum convolved with NEAR unfiltered detector response function; solid curve is total x-ray spectrum, dashed curve is coherently-scattered portion of spectrum. Vertical dashed lines indicate positions of Kα x-ray lines for (left-to-right) Mg, Al, Si, S, Ca and Fe. Under quiet Sun conditions (~5 MK), significant signal is predicted only below ~3 keV. Under flare conditions (*e.g.*, 16 MK), hardening of the solar spectrum leads to observable Ca and Fe fluorescence. Scattered photons make up a significant proportion of total predicted flux in the Al, S, and Ca lines.

These compositions were taken from a large database of meteorite bulk compositions developed to aid in the interpretation of NEAR XGRS data (Nittler *et al.*, 2000). Theoretical x-ray spectra were convolved with the response functions of the three asteroid-pointing detectors to generate synthetic NEAR spectra. The Al-filtered spectra included the filter enhancement effect described earlier. The model spectra were then fitted to derive photon ratios, using the same fitting technique used to fit actual NEAR spectra. By fitting polynomial curves to plots of predicted photon ratios *vs.* elemental ratios for the meteorite compositions, calibration curves were derived and used to convert photon ratios to elemental abundance ratios for the actual NEAR spectra. Example calibration curves for Mg/Si and Fe/Si for a few solar temperatures are shown in Fig. 6.

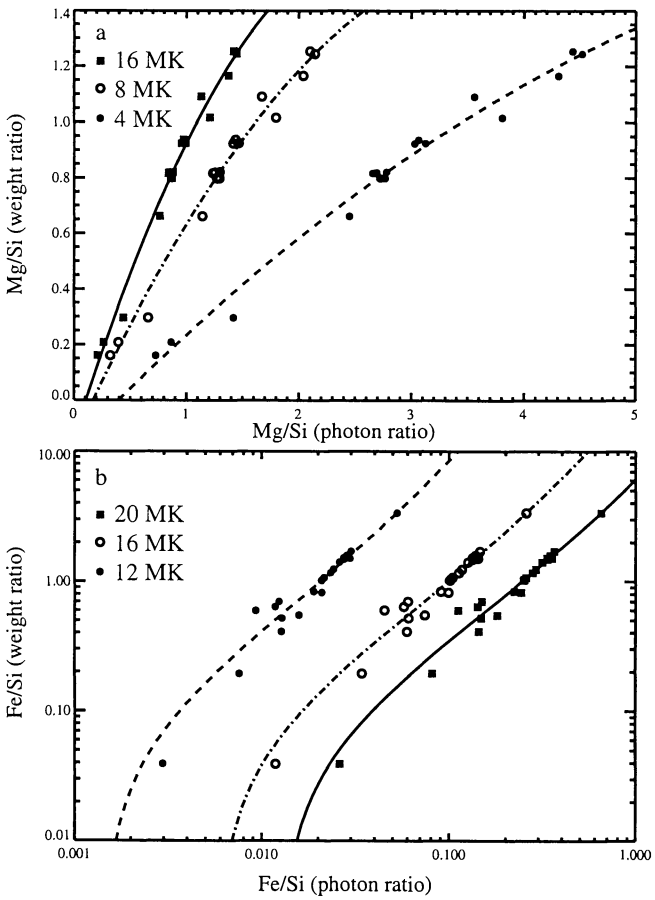

FIG. 6. Theoretical calibration curves relating x-ray photon ratios to concentration ratios for (a) Mg/Si and (b) Fe/Si, for a range of solar temperatures. Symbols are results of model calculations for specific meteorite compositions; curves are second-order polynomial fits to the points. Each set of symbols and curve corresponds to the indicated solar temperature. Mg/Si photon ratios decrease and Fe/Si ratios increase with increasing solar temperature, reflecting the spectral hardening of the solar x-ray spectrum with temperature. Similar calibration curves were used to derive Al/Si, S/Si and Ca/Si ratios.

Note that these models assume that the sample being analyzed is homogeneous in composition, but in reality the surface of Eros probably consists of grains of different minerals. Assuming the typical grain size is larger than the mean free path of the x-rays (<10 μm for Mg, Al and Si, <100 μm for Fe), and different elements are primarily concentrated in different minerals, this could have large effects on the fluorescent x-ray spectra. For example, essentially all Al in ordinary chondrites is present in feldspar. In modeling x-ray emission from an assumed homogeneous chondritic composition, a significant portion of the fluorescent Al photon flux is absorbed on the way out of the surface by the highly abundant Mg. In feldspar, however, the Al x-ray flux should be largely unattenuated, and for the same bulk composition a higher Al flux observed. We do not know the exact compositions and relative abundances of different minerals for the meteorites in our database. However, to address this issue we calculated nominal elemental abundances for typical H, LL and R chondrites and a eucrite. Each meteorite was assumed to consist of mixtures of olivine, pyroxene, feldspar, Fe-Ni metal and iron sulfide. Typical mineral abundances and relative proportions were taken from the literature and combined to give an appropriate whole-rock composition. We computed models for the mineral compositions individually for a range of solar temperatures and combined the resulting spectra according to their relative concentration, by volume, in the whole rock. This assumes that the relative surface area of the minerals on the surface of Eros is equal to their volume percentage. Photon fluxes and ratios were derived from the combined spectra and compared with those derived from the homogeneous model.

Results, in the form of ratios of photon ratios derived from the homogeneous composition to those derived from the mineral mixture, are given in Table 2. These ratios were found to be independent of solar temperature. The magnitude of the mineral mixing effect for chondrites ranges from 5 to 10% for Mg/Si to ~30% for Al/Si. The effect on Fe/Si can be even larger and depends on the amount of iron present in metallic form: the R- and H-chondrite models have similar bulk Fe, but quite different predicted Fe/Si photon ratios. Clearly, our inferred elemental ratios for Eros should be corrected to take this effect into account. The variability in the magnitude of the effect between different meteorite types is troubling, however, since it likely represents a limit on how accurately the surface composition of Eros can be determined by remote-sensing techniques without accurate knowledge of mineral compositions and abundances. This knowledge is probably not attainable without detailed exploration of the surface itself or sample return. In this paper, we correct the elemental ratios derived for flares from the model calibration curves using the average ratios for the three chondrite types; these correction factors are given in the last column of Table 2. The standard deviations of these correction factors can be taken as relative systematic uncertainties in our derived abundance ratios.

An additional source of systematic uncertainty in our analyses is the variability of elemental abundances in the solar corona. The solar models used to calculate calibration curves and used in the solar monitor fitting assume a specific set of coronal elemental abundances (Meyer, 1985). However, many different solar observations indicate that the elemental abundances in the corona can vary strongly with time. For example, Antonucci and Martin (1995) found that the Fe/Ca ratio can vary by a factor of 4 between different large flares, and Sylwester *et al.* (1998) found that the absolute Ca abundance varied by a factor of ~3.5 between flares. For a given temperature, the solar x-ray continuum should be constant. However, variations in abundances will cause variations in line intensities, in turn leading to variable fluorescence intensities from the asteroid. Some of the discrepancy between our modeled and observed solar spectra probably does reflect such variations. For example, the observed solar monitor spectrum for the 2000 December 27 flare (Fig. 2d) shows excess signal ~3 keV, compared with the other flare spectra, perhaps due to enhanced Ar or K abundance in the coronal plasma. This is discussed in more detail in the next section.

To assess the magnitude of the expected variability, we calculated 100 x-ray models for an LL-chondrite composition and a 16 MK Sun. For each model, individual elemental abundances (C-Ni) were independently and randomly chosen from Gaussian distributions about their nominal coronal values. The widths of the distributions were taken to be 10% of the mean abundance; this reproduced well the observations of Antonucci and Martin (1995) and Sylwester *et al.* (1998) for Fe and Ca abundances. The resulting Mg/Si, Al/Si, S/Si, Ca/Si and Fe/Si photon ratios predicted from synthetic NEAR spectra

TABLE 2. Effect of assumed heterogeneous (mineral mixing) *vs.* homogeneous compositions for predicted x-ray fluorescence photon ratios.

Ratio	Ratio of homogenous model to mineral mixing model				
	R chondrite	LL chondrite	H chondrite	Eucrite	Chondrite average
Mg/Si	1.11	1.05	0.95	1.23	1.04 ± 0.08
Al/Si	0.70	0.76	0.80	0.71	0.76 ± 0.05
S/Si	1.28	1.29	1.45	1.08	1.34 ± 0.10
Ca/Si	1.05	1.08	1.25	0.95	1.12 ± 0.10
Fe/Si	1.18	1.29	1.78	1.20	1.42 ± 0.32

varied about the mean by ~10%. Thus, even with a perfectly homogeneous asteroid and a constant solar temperature, solar abundance variations would be expected to lead to this level of heterogeneity in derived elemental ratios, unless the variations were observable and corrected for in the solar monitor data.

RESULTS

Derived photon and elemental ratios for the five flares and two quiet Sun integrations are presented in Table 3. For each flare, two sets of element ratios are given, corresponding to the two solar monitor fits: the two-temperature fit to the entire spectrum (F1) and the fit to just the high-energy region of the solar spectrum (F2). The element ratios are plotted in Fig. 7.

For most flares, the results using the two solar fits are quite different, especially for Fe/Si and Ca/Si ratios. This reflects the fact that, in the two-temperature (F1) model, the low-temperature component increases the flux of Si fluorescence photons and increases the predicted Mg/Si photon ratio without affecting the Fe or Ca fluxes. As a result, the Fe/Ca ratio derived for the flares is essentially identical for the two fits while the ratios relative to Si vary. This is illustrated in Fig. 8 where the Fe/Si ratios are plotted *vs*. Fe/Ca ratios for the four flares with Fe and Ca signals. For each flare, the ellipse with the higher Fe/Si ratio corresponds to the F1 fit. Also shown are these ratios for a large number of meteorites of widely varying type. Although there is a wide range of inferred Fe/Si ratios, it is noteworthy that at least one fit from each flare lies in the region of the plot occupied by ordinary chondrites. For the flares from May 4 and June 15, the F2 fit gives approximately chondritic Fe/Si while the F1 fit gives much higher Fe/Si. For the December 27 flare, it is the F1 fit that gives chondritic Fe/Si and the F2 results are much lower. Both fits from January 2 give chondritic ratios.

The lower Fe/Si and Ca/Si ratios inferred for the December 27 flare compared to the other data is likely due to incorrect modeling of the solar spectrum. As mentioned above, the solar x-ray spectrum for this flare contains significantly higher flux ~3 keV compared to the other flares, perhaps indicating an

TABLE 3. Derived photon and elemental abundance ratio data for Eros.*

Spectrum	Ratio	Mg/Si	Al/Si	S/Si	Ca/Si	Fe/Si
2000 May 4	Photon	0.93 ± 0.03	0.08 ± 0.02	0.055 ± 0.007	0.052 ± 0.004	0.101 ± 0.004
Flare	Element: F1	0.64 ± 0.02	0.04 ± 0.02	0.049 ± 0.015	0.201 ± 0.026	4.32 ± 0.22
	Element: F2	0.88 ± 0.03	0.04 ± 0.02	0.026 ± 0.008	0.081 ± 0.010	2.03 ± 0.10
2000 June 15	Photon	0.96 ± 0.070	0.12 ± 0.05	0.023 ± 0.017	0.047 ± 0.012	0.077 ± 0.009
Flare	Element: F1	0.70 ± 0.05	0.081 ± 0.045	0.004 ± 0.011	0.152 ± 0.066	3.12 ± 0.46
	Element: F2	0.90 ± 0.06	0.083 ± 0.045	0.001 ± 0.009	0.079 ± 0.034	1.75 ± 0.24
2000 July 10	Photon	1.16 ± 0.05	0.10 ± 0.04	0.009 ± 0.014	–	–
Flare	Element: F1	0.86 ± 0.04	0.06 ± 0.03	0.0004 ± 0.0004	–	–
	Element: F2	1.07 ± 0.04	0.07 ± 0.03	<0.004	–	–
2000 December 27	Photon	0.97 ± 0.04	0.08 ± 0.03	0.064 ± 0.008	0.054 ± 0.005	0.105 ± 0.005
Flare	Element: F1	0.81 ± 0.03	0.05 ± 0.03	0.047 ± 0.013	0.082 ± 0.012	1.32 ± 0.08
	Element: F2	0.97 ± 0.04	0.05 ± 0.03	0.032 ± 0.009	0.043 ± 0.007	0.75 ± 0.04
2001 January 2	Photon	0.93 ± 0.04	0.14 ± 0.03	0.036 ± 0.010	0.045 ± 0.007	0.080 ± 0.005
Flare	Element: F1	0.84 ± 0.03	0.10 ± 0.03	0.011 ± 0.009	0.077 ± 0.020	1.69 ± 0.12
	Element: F2	0.89 ± 0.04	0.10 ± 0.03	0.010 ± 0.008	0.067 ± 0.017	1.48 ± 0.11
Quiet Sun	Photon	2.19 ± 0.08	0.16 ± 0.04	–	–	–
summer	Element	0.72 ± 0.10	0.05 ± 0.03	–	–	–
Quiet Sun	Photon	2.44 ± 0.11	0.19 ± 0.05	–	–	–
winter	Element	0.70 ± 0.11	0.05 ± 0.03	–	–	–
Best Eros	Element	0.85	0.068	<0.05	0.077	1.65
σ	–	0.11	0.022	–	0.006	0.27
σ_{mean}	–	0.04	0.007	–	0.003	0.12

*For solar flares, element ratios were derived for two theoretical solar spectra: F1, two-temperature fit to solar monitor; F2, single temperature-fit to high energy portion of solar monitor (see text). Element ratios for quiet Sun were derived using GOES temperatures (Table 1). All element ratios are weight ratios.

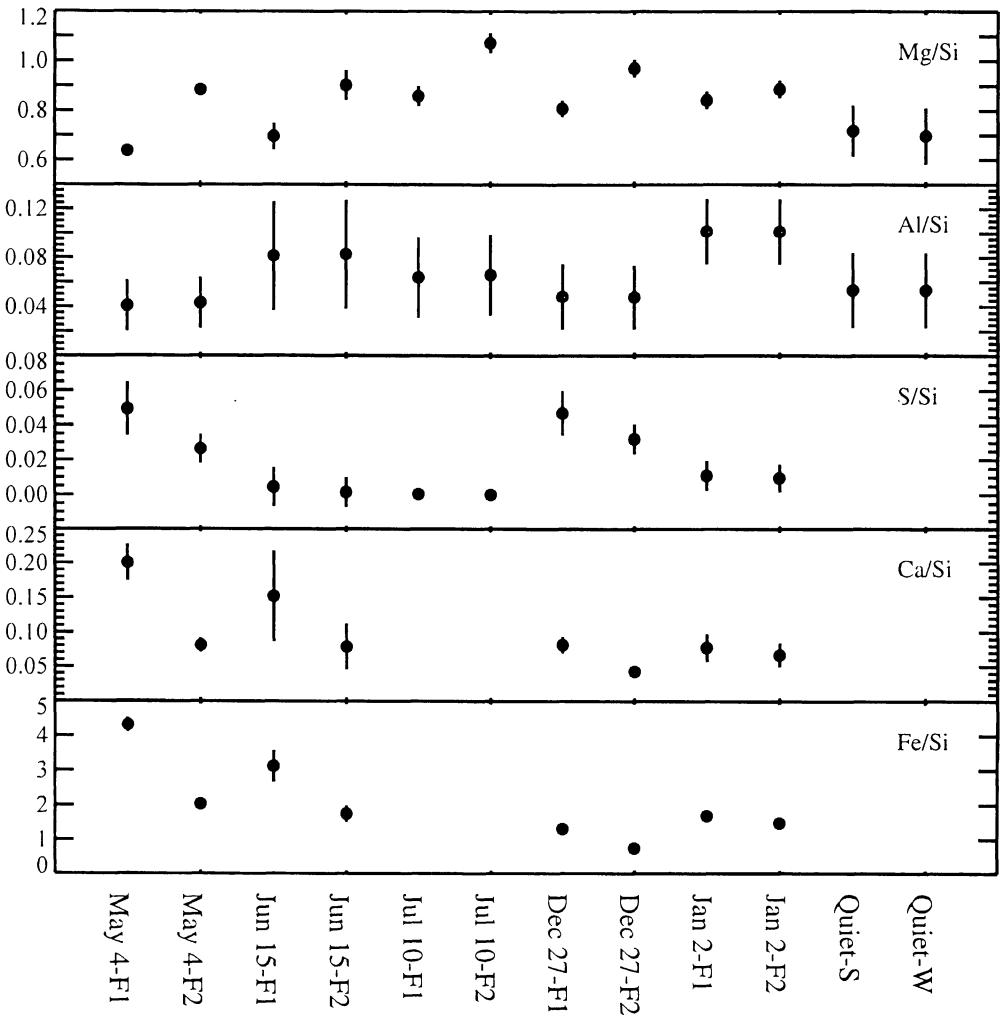

FIG. 7. Element-ratio results for five solar flares and two quiet Sun spectral sums. Two sets of results are plotted for each flare: F1 corresponds to results calculated using two-temperature fits to the solar monitor spectra; F2 indicates results from single high-temperature fits. See text for details.

increased abundance of K or Ar in the solar corona. This flux was not taken into account in the modeling used to convert photon ratios to abundance ratios. However, the excess solar flux lies below the Ca line and would thus be expected to increase the flux of Mg, Al, Si and S without affecting Ca or Fe. In particular, this would indicate we have underestimated the Fe/Si and Ca/Si ratios for this flare. Continued modeling of the solar spectrum for this flare is obviously needed.

It is clear at this point, given the uncertainties remaining in the solar monitor response function and the possibility of elemental variations in the Sun, that we have very large absolute uncertainties in our derived element ratios for Eros, especially for Fe/Si and Ca/Si. However, we argue here on cosmochemical grounds in fact the convergence of many results near the ordinary chondrites suggests that in fact this is the true composition of Eros. The strongest argument is perhaps the chondritic Fe/Ca ratio derived for the flares regardless of solar fit. As can be seen in Fig. 8, the classes of meteorites that have Fe/Ca ratios between 10 and 20 include chondrites, mesosiderites, diogenites, and several classes of primitive achondrites. Despite the two flare analyses that plot near the mesosiderites, it is highly unlikely that Eros is related to these stony-iron meteorites. Mesosiderites are mixtures of basaltic material and Fe-Ni metal and have much higher Al/Si ratios and lower Mg/Si ratios than the XRS data indicates for Eros (Table 3; Figs. 7 and 9). Moreover, the mesosiderites have Fe/Ca ratios that range to much higher values than observed for Eros. We argue that the high apparent Fe/Si ratios for these two analyses reflect an error in fitting the low-energy portion of the solar monitor. The lower-than chondritic Fe/Si ratio of the F2 fit for the December 27 flare is intermediate between chondrites and diogenites and is similar to some ureilites. Again, independent data argue against a connection between Eros and these types of rocks. Diogenites are pyroxenites and are clearly

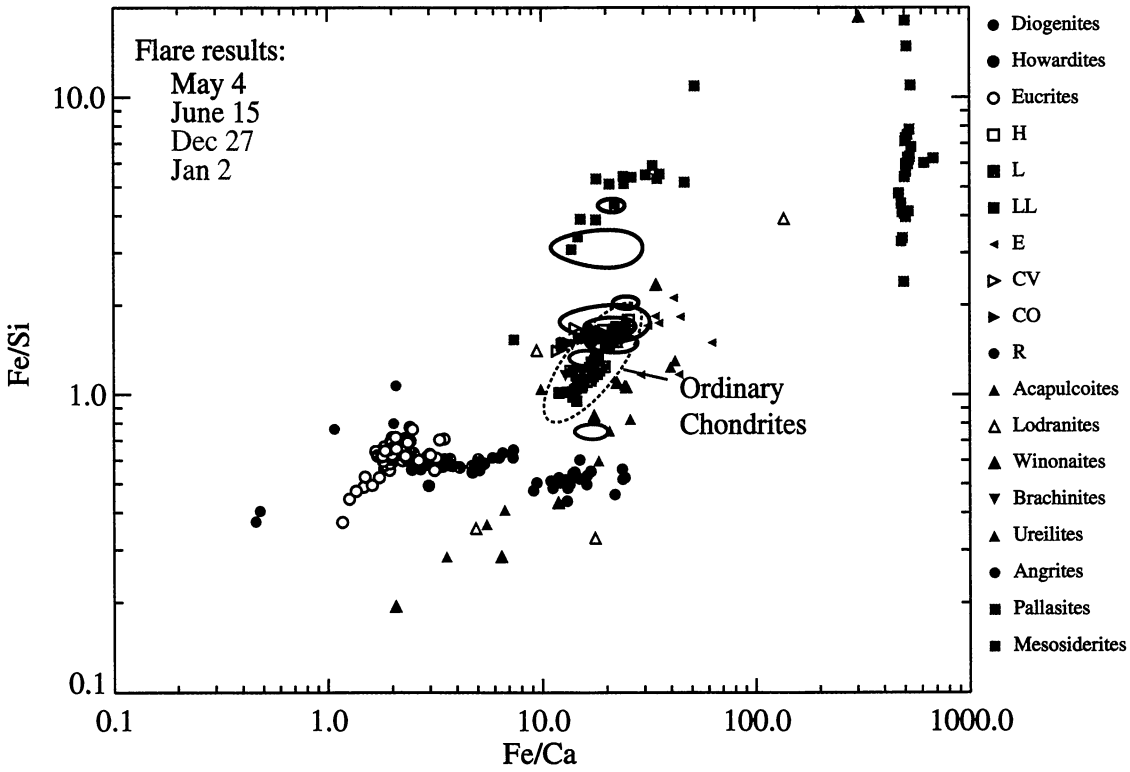

FIG. 8. Fe/Si and Fe/Ca weight ratios inferred for Eros from four solar flares and measured in the laboratory for different types of meteorites. Meteorite data in this and subsequent figures are taken from a large database of laboratory data (Nittler *et al.*, 2000). Two 1σ error ellipses are plotted for each flare. The ellipse with higher Fe/Si is the F1 (two-temperature) solar monitor fit; the other is the F2 (single-temperature) fit. The Fe/Ca ratios are mostly independent of the fit and are similar to ordinary chondrites. In contrast, Fe/Si ratios vary strongly between fits, but at least one ellipse from each flare lies close to the H-chondrite field. The fits that best match chondritic Fe/Si also result in a Mg/Si ratio close to ordinary chondrites. We argue that this convergence of the data indicates that Eros has approximately chondritic Mg/Si, Fe/Si and Fe/Ca ratios. The discrepant data points with high and/or low Fe/Si ratios are probably due to systematic errors in fitting solar monitor spectra, due to incomplete understanding of the solar monitor graded shield.

excluded by data from the NEAR NIS, which shows conclusively that there is a significant amount of olivine at the surface of Eros (Veverka *et al.*, 2000; Lucey *et al.*, 2001). The ureilites that have low Fe/Si typically have higher Mg/Si ratios than we have determined for Eros. Also, as discussed above, we think that it is likely that the low Fe/Si for this flare is an artifact of not taking into account the excess 3 keV flux in the solar spectrum. Finally, the fact that both fits for the January 2 flare yield a chondritic composition also argues that this is the actual composition of Eros.

Based on the above arguments, we assume for the rest of this paper that the flare analyses with high Fe/Si (May 4 F1, June 15 F1) and low Fe/Si (December 27 F2) are erroneous and the remaining data points represent our best measure of the true surface composition of Eros. Some of the spread in the remaining data points could reflect elemental heterogeneity on Eros. We think this is unlikely, however, due to the extreme homogeneity of the mafic mineralogy as determined by the NEAR NIS (Veverka *et al.*, 2000). We thus assume here that Eros is largely homogeneous and determine an average composition from the remaining data points (last row of Table 3). The average elemental ratios are given in the last row of Table 3, together with the standard deviations and standard errors of the mean. The standard deviation is a measure of the range of compositional variability allowed by the data; the standard error of the mean is a better indicator of our uncertainty in the average composition. The uncertainty in the mineral mixing correction (Table 2) was not propagated in these calculations. Systematic errors in this correction would change the absolute values of the ratios but not the relative size of the error bars. Finally, the average S/Si ratio is 0.014 ± 0.017 (1σ). Because this ratio is within 1σ of zero, we report an upper limit for S/Si determined by adding 2σ to the average ratio. This upper limit is close to the maximum value measured for an individual flare spectrum.

The average elemental ratios are plotted as 2σ error ellipses, together with a large number of meteorite classes, in Figs. 9–13. The larger ellipses represent the standard deviation of the individual flare analyses, reflecting the allowed compositional variability. The smaller ellipses are the σ_{mean} values and indicate our uncertainty in the average composition. The results are broadly consistent with our preliminary results reported by Trombka *et al.* (2000).

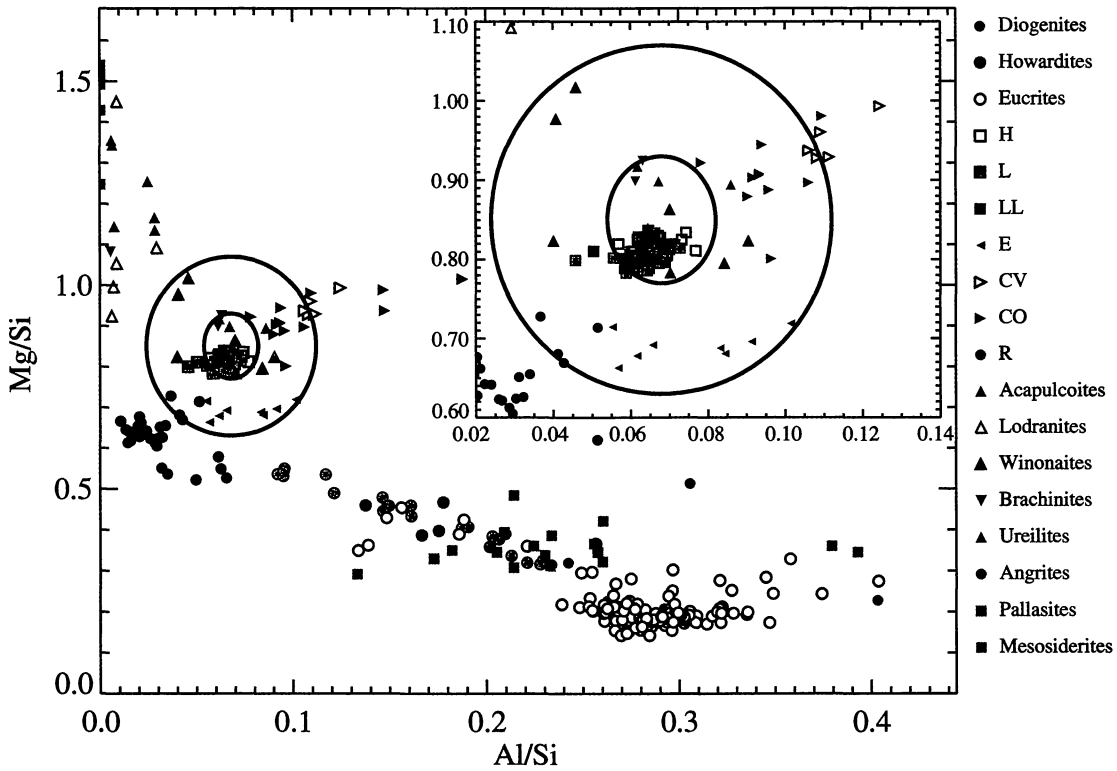

FIG. 9. Average Mg/Si and Al/Si weight ratios of Eros, plotted with a large number of meteorites. The larger error ellipse indicates the 2σ variability in the data; this is the allowed range of elemental heterogeneity between the sampled regions of Eros. The smaller ellipse represents 2× the standard error of the mean and represents the uncertainty in our knowledge of the average composition. The inset expands the chondritic region of the plot. The approximately chondritic Mg/Si and Al/Si abundance ratios rule out the possibility of global differentiation of Eros. However, the Eros error ellipses include several classes of chondrites as well as partially-differentiated primitive achondrites (*e.g.*, acapulcoites, winonaites).

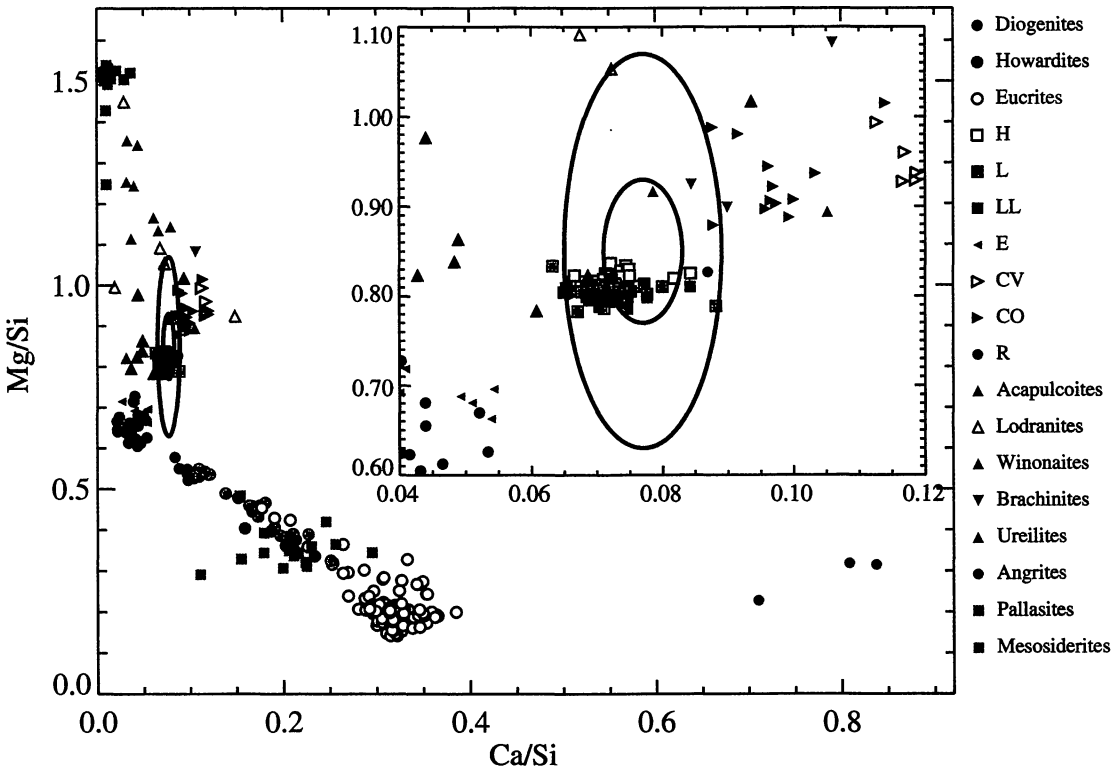

FIG. 10. Average Mg/Si and Ca/Si weight ratios of Eros (ellipses), plotted with a large number of meteorites. See Fig. 9 for explanation of error ellipses. The inset expands the chondritic region of the plot. As for Al/Si, the Ca/Si ratio rules out global differentiation, but the data allow for several primitive meteorite classes to be potential analogs of Eros.

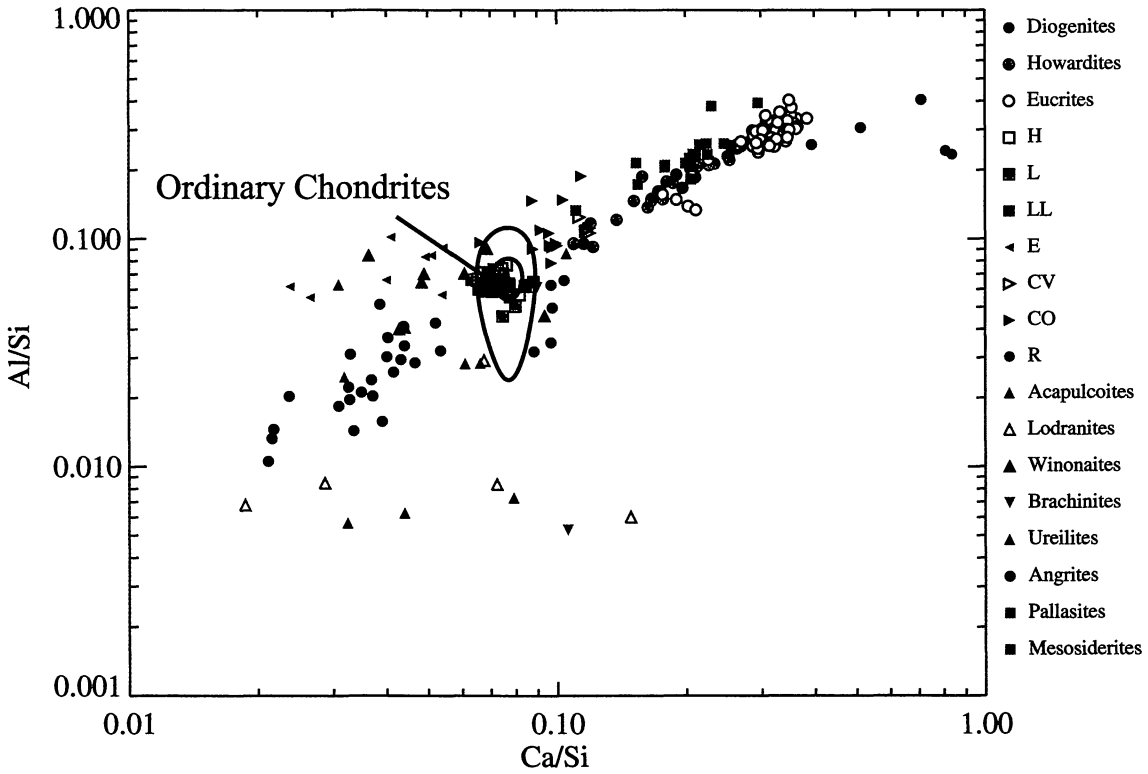

FIG. 11. Average Al/Si and Ca/Si weight ratios of Eros (ellipses), plotted with a large number of meteorites. See Fig. 9 for explanation of error ellipses. Al and Ca abundances are highly correlated between different meteorite classes.

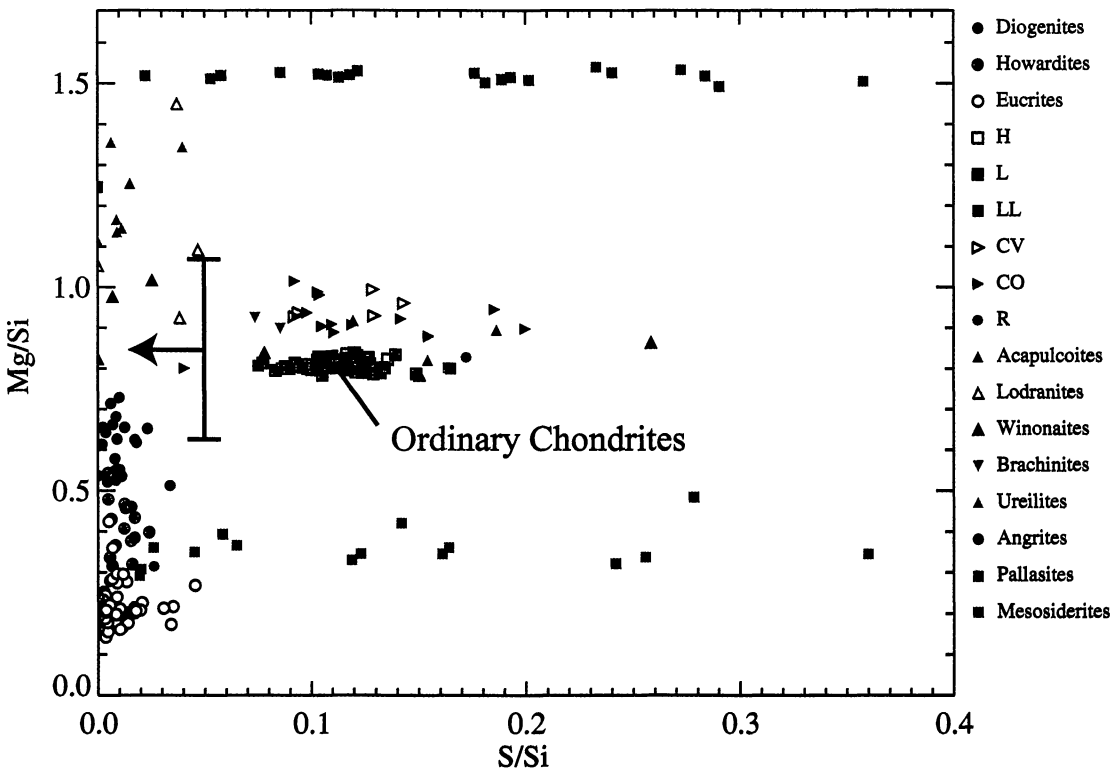

FIG. 12. Mg/Si and S/Si weight ratios of Eros, plotted with a large number of meteorites. The S/Si ratio is at least a factor of 2 lower than observed in unweathered chondrites, probably reflecting surface depletion of sulfur, due to processing by impacts and/or radiation.

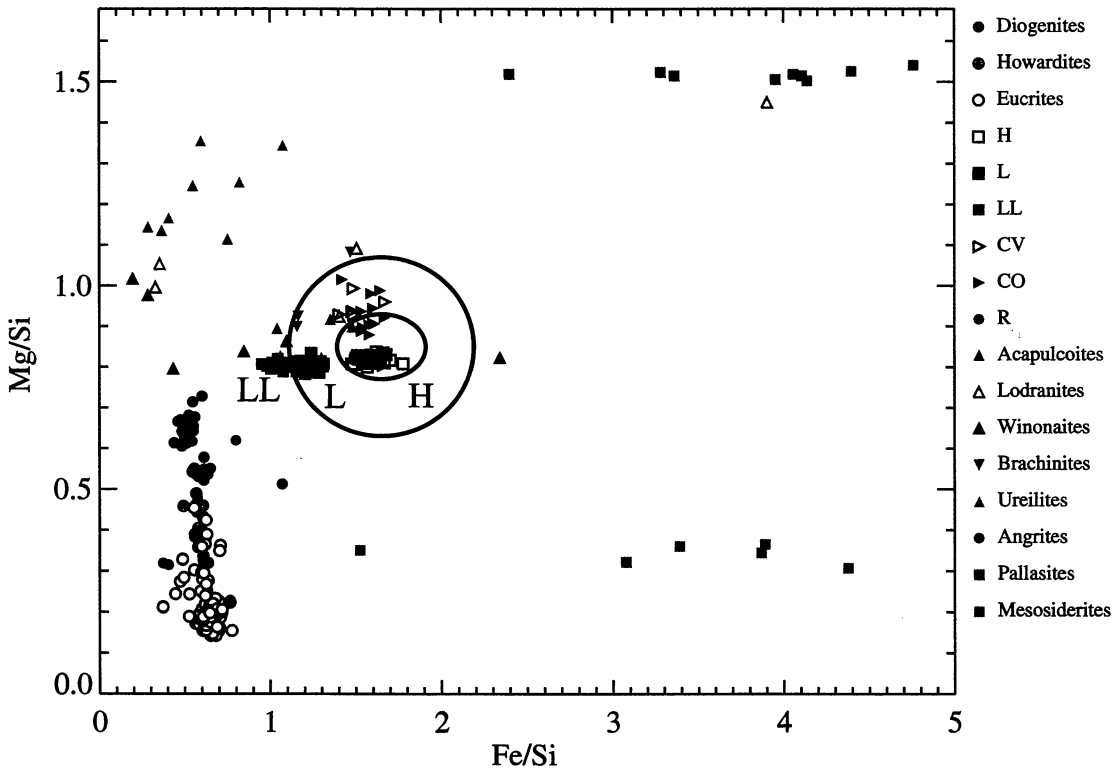

FIG. 13. Average Mg/Si and Fe/Si weight ratios of Eros (ellipses), plotted with a large number of meteorites. See Fig. 9 for explanation of error ellipses. The Eros data most closely overlap H, R and L chondrites. However, remaining uncertainties in fitting NEAR solar monitor spectra (see Fig. 8 and text) and in correcting for a heterogeneous composition suggest that the true Fe/Si error bar might be larger than we have indicated. Moreover, lack of understanding of asteroid regolith processes probably precludes accurate determination of the bulk Fe/Si ratio by remote-sensing techniques.

Mg/Si, Al/Si and Ca/Si ratios are shown in Figs. 9, 10 and 11. These three ratios measured for Eros are in excellent agreement with those observed in ordinary chondrites, though the 2σ errors include a number of other meteorite types as well. The low Mg/Si and very high Al/Si and Ca/Si ratios observed in basaltic meteorites from the crusts of differentiated asteroids (*e.g.*, eucrites, angrites) are completely ruled out by our data. Similarly, the measured Mg/Si ratio is lower than that measured in the olivine-rich residues of partial melting (ureilites, lodranites) and stony-iron pallasites. We note that Trombka *et al.* (2000) reported a very low Mg/Si element ratio of ~0.6 for a flare that occurred on 2000 July 19. We do not report data for this flare here because of difficulties outlined earlier. However, it is worth noting that a re-analysis of this flare spectrum using the refined techniques used in this paper yields a higher Mg/Si ratio, in the range of the other flare results, for any reasonable choice of background and solar temperature. The low initial result appears to have been an artifact of the matrix-inversion technique used by Trombka *et al.* (2000).

Figure 12 shows Mg/Si plotted *vs.* S/Si for Eros and several meteorite classes. Trombka *et al.* (2000) reported upper limits on the S/Si ratios for two solar flares observed by the NEAR XRS, suggesting at least an order of magnitude depletion of S at the surface of Eros. The upper limits were based on our x-ray models at the time, which predicted higher S/Si photon ratios than were observed, even for a sulfur-free composition. However, subsequent to publication it was discovered that our model overestimated the scattered solar x-ray flux, and the model S/Si photon ratios were consequently too high. Our current models still yield low S/Si element ratios (Figs. 7 and 12) but the 2σ upper limit is higher than that reported in Trombka *et al.* (2000). As shown in the synthetic 16 MK LL chondrite spectra in Fig. 5c, much of the predicted flux in the vicinity of the S line at 2.3 keV is due to coherently scattered solar x-rays, and we must address the possibility that the apparent low S/Si ratio is an artifact of errors in the scatter model. To bring the S/Si ratio inferred for Eros up to that of ordinary chondrites (~0.1) would require that the scattered flux at ~2 keV be essentially zero. We think such a gross error in the scatter model is highly unlikely both because this would also strongly affect the Al and Ca abundances and because the magnitude of the predicted scattered continuum between 4 and 6 keV is in excellent agreement with that observed in this energy region in the unfiltered detector spectra for the solar flares. We thus conclude that the low S/Si ratio at the surface of Eros is real and probably reflects a depletion of sulfur from a primitive composition. This is discussed further in the following section.

The Mg/Si ratio is plotted *vs.* the Fe/Si ratio in Fig. 13. The Fe/Si ratio closely agrees with that measured in H chondrites, but other classes are allowed within the error bars. The true error bar on Fe/Si is in fact larger than we have estimated here because of the large range of mineral mixing correction factors determined for different classes of chondrites (Table 2) and because of residual problems with solar monitor modeling.

DISCUSSION

One of the primary goals of the NEAR mission has been to determine whether Eros is related to any of the known asteroid samples on earth, the meteorites. We have no reason *a priori* to believe that we have any samples of Eros in our collections. In fact, the delivery and survival of meteorites is a highly random and biased process and there are likely to be a great many asteroids for which we have no samples in the laboratory. That said, the spectral similarity between individual members of asteroid classes indicates that there are common processes of origin and evolution that affect many asteroids. The similarity of Eros to many other S-class asteroids suggests that it has a similar composition to these and may be used as a proxy for the S(IV) asteroid class, both for identification of likely meteorite analogs and for deciphering geological histories. Since this class has been suggested to include the parent bodies of the ordinary chondrites (Gaffey *et al.*, 1993a,b), which dominate the flux of meteorites onto the Earth, a critical question is whether the compositional data we report here support such a connection.

Meteorite classes can be broadly divided into four groups: (1) achondrites, including howardites, eucrites, diogenites, and angrites; (2) stony-iron meteorites, including the pallasites and mesosiderites; (3) primitive achondrites, including acapulcoites, lodranites, brachinites, ureilites, winonaites and a few other rare types; and (4) primitive meteorites, including the ordinary, enstatite, carbonaceous and R chondrites. Representative compositions of all of these meteorite classes are plotted along with the XRS results from Eros in Figs. 8–13; these data are taken from our bulk-composition meteorite database (Nittler *et al.*, 2000).

The XRS data completely rule out the possibility of global differentiation on Eros. Howardites, diogenites, eucrites and angrites, thought to represent material from near the surface of differentiated asteroids, have Mg/Si, Al/Si and Ca/Si ratios that lie almost exclusively outside the error ellipses for the XRS data in Figs. 9–11. A few diogenites slightly overlap the Mg/Si and Al/Si ratios for Eros (Fig. 9). However, these points are excluded by the Ca/Si and Fe/Si ratios. Moreover, diogenites, which are almost exclusively composed of pyroxene, can be ruled out as analogs of Eros on the basis of reflectance spectroscopy (Veverka *et al.*, 2000; Lucey *et al.*, 2001). At the other end of the spectrum, meteorites from the cores and mantles of differentiated asteroids are also excluded by the XRS results. For example, the olivine-rich pallasites have Mg/Si ratios much higher than that inferred for Eros.

The NEAR XRS measurements of Eros thus point to a primitive, largely undifferentiated composition for the asteroid. A large number of meteorite classes have bulk compositions that can be characterized as primitive, but the errors in the XRS determinations allow us to narrow down the potential meteorite analogs considerably. In fact, for all but the S/Si ratio, the measured ratios are in excellent agreement with the ordinary chondrites and exclude almost all carbonaceous chondrites. If we take the standard error of the mean as our uncertainty in the determination of the average elemental ratios for Eros, the data favor the high-iron H subclass. However, even this more restrictive error bound still allows other meteorite classes to be considered as potential analogs, including the R chondrite Rumuruti (Kallemeyn *et al.*, 1996) and several classes of primitive achondrites, so a direct link to H chondrites is not required by the data. Enstatite chondrites have Mg/Si ratios at the very low end of our allowed value. However, these meteorites are ruled out as potential analogs to Eros by their lack of FeO-rich mafic silicates, which is in inconsistent with infrared observations (Veverka *et al.*, 2000). Although our derived Fe/Si ratio is most consistent with H or R chondrites, if we consider the large systematic errors from modeling solar spectra and mineral mixing, even the low-iron L and LL ordinary chondrites could be accommodated by our data. As discussed below, however, regolith processes could lead to a surface Fe/Si ratio different from that of the bulk asteroid, however.

The S/Si ratio is crucial for determining meteorite analogs to Eros and for unraveling the geological history of the asteroid. Trombka *et al.* (2000) provided three possible explanations for the low measured S/Si ratio: (1) It is a primary feature of the primitive material that accreted to form the asteroid; (2) it reflects a low level of partial melting, with accompanying loss of a FeS-rich melt; or (3) it reflects volatilization of iron sulfide and loss of S at the asteroid's surface due to bombardment by micrometeorites or radiation. Which, if any, of these explanations is correct would have significant implications for the cosmochemical and geological history of Eros. For example, if the low S/Si ratio is primordial, it indicates that Eros accreted from material strongly fractionated from any known primitive solar system material. If, instead, the low S/Si ratio indicates sulfur depletion from chondritic starting material, explanation (2) would require that Eros has undergone significant heating and partial melting, whereas explanation (3) would allow the asteroid to have remained unheated. Let us examine these possibilities in more detail.

We consider it highly unlikely that the low S/Si ratio is primordial. Our meteorite database contains laboratory measurements of S/Si ratios for 380 chondrite falls sampling essentially all chondrite classes (Nittler *et al.*, 2000). The minimum observed value is 0.075, higher than the upper limit determined for Eros. A few meteorites have lower ratios, but all are heavily weathered finds. Interplanetary dust particles, which are among the most primitive materials available for study and likely sample a wide range of parent bodies (Bradley *et*

al., 1988), are also universally rich in S, arguing against the existence of S-poor primitive parent bodies in the inner solar system.

As a rock of chondritic composition is heated, the first partial melt to form is at the Fe,Ni-FeS cotectic and contains ~85 wt% FeS or ~30 wt% S (Kullerud, 1963). Subsequent removal of this melt could produce substantial S depletions. Loss of this partial melt would also decrease the Fe/Si ratio by ~15%. Various levels of parent-body partial melting and melt separation are represented in the meteoritic record by the primitive achondrites (Mittlefehldt *et al.*, 1998). For example, the acapulcoites and lodranites are classes of strongly heated meteorites believed to have originated on the same parent body. Acapulcoites have bulk element compositions similar to chondrites, indicating a low level of melt segregation. In contrast, the lodranites are clearly residues of partial melting and have low S/Si ratios (Fig. 12), within the range allowed by the XRS data. However, it is unclear whether an Fe,Ni-FeS partial melt could be efficiently separated from the unmelted portion of a chondritic rock without at least some accompanying silicate melting. The lodranites and other primitive achondrites (*e.g.*, ureilites) that have lost FeS-rich partial melts also usually show evidence for having lost silicate partial melts, namely increased Mg/Si ratios and decreased Al/Si and Ca/Si ratios (Figs. 10 and 11). The Mg, Al and Ca compositions of the S-depleted primitive achondrites do not in general overlap the XRS results, arguing against a partial melting explanation for the low S/Si ratio of Eros. Moreover, McCoy *et al.* (2000) argued that partial melting as reflected in the acapulcoites and lodranites should lead to high levels of observable mineralogical and elemental heterogeneity on a scale of kilometers at the surface of asteroids. Our error bars do allow a certain level of elemental heterogeneity, but the observed range of element ratios in the primitive achondrites is typically larger than our error bounds for most ratios. The high degree of homogeneity in the mafic mineralogy of Eros also argues against significant partial melting (Veverka *et al.*, 2000). We note that regolith mixing could reduce the extent of surface elemental variability, however, so the observed elemental and mineralogical homogeneity does not unambiguously rule out partial melting.

Surfaces exposed to space are modified by interactions with radiation, ions and impacting meteors. These processes, often referred to as "space weathering", are now reasonably well understood on the Moon (Pieters *et al.*, 2000), but far less so for asteroids. Because the x-rays observed by the NEAR XRS are produced in the upper ~100 μm of the regolith, it is possible that the observed S depletion is purely a surface effect due to space weathering of some sort (Trombka *et al.*, 2000). Because of its high volatility, sulfur would be expected to be lost more easily during such processes than other elements. We have calculated rates of photosputtering, ion-sputtering and impact vaporization at Eros, and have obtained a range of plausible erosion rates. We assumed a photo-sputtering efficiency of 1.15×10^{-21}/UV photon, and that the effective solar photon flux at Earth orbit is 1×10^{14} photons cm^{-2} s^{-1}. We assume that the efficiency for ion sputtering is 0.15 per solar wind particle on average. This is a conservative estimate: although the sodium sputter yield of 5 keV protons is 0.2, that of 5 keV α particles is 1.3 and that of Ar is 22 from the yields in Matsunami *et al.* (1984). The impact vaporization has been calculated in two ways. First, we use the planar impact approximation (Melosh, 1989) as described in Morgan and Killen (1998) and Killen *et al.* (2001). Second, we calculate the total mass of melt plus vapor given by Pierrazo *et al.* (1997). We assume the material properties of anorthosite, a density of 1.8 g/cm^3 for the asteroid surface and 3.1 for the impactor, and the velocity distribution of meteoroids from Erickson (1968). The results of our planar impact approximation agree with the more rigorous calculations of Cintala (1992) for the same input conditions. The melt plus vapor gives 30× the mass of the planar approximation. There is probably an order of magnitude more vapor in the vapor plus melt phase than in the pure vapor phase. Photo-sputtering yields ~56× more vapor, and ion sputtering ~40× more, than the plane parallel impact calculation. These results undoubtedly bracket the solution. If Eros has been at an average orbital distance of 1.5 AU and had an initial sulfur abundance of 2%, then the erosion rate of sulfur is calculated to be 3–4 monolayers per year for sputtering plus impact vaporization. Given a steady loss rate, the upper 1 cm could be completely depleted in sulfur over 10 Ma. Given that the total amount of melt is a factor of 30× greater than the impact vapor, if the sulfur in this melt vaporizes, then the loss rate could be correspondingly higher. The estimated uncertainty on these calculations is roughly a factor of 2. Loss of the other elements measured by the XRS would also be expected due to these processes, but the level of depletion of these elements should be much lower than that of S since they are much less volatile. Further calculations are in progress to quantify this statement.

The above calculations confirm that impact-induced volatilization and sputtering can indeed plausibly account for the loss of sulfur observed on the surface of Eros. This is our favored explanation for the low measured S/Si ratio. Note that the several million-year timescale for sulfur depletion suggests the possibility of S/Si variability at the surface, correlated with age of the exposed regolith. Recently exposed material would be expected to have a chondritic S/Si ratio while older, more weathered regions should be depleted in sulfur. Albedo and color variations observed with the NEAR MSI indicate the existence of materials on Eros' surface with different levels of alteration from exposure to space (Veverka *et al.*, 2000, 2001; Robinson *et al.*, 2001). Because the spatial scale of such variations is in general smaller than the XRS footprint, it would be difficult to directly correlate S/Si ratios determined by the XRS with the surface properties observed by the MSI. Nonetheless, there is a hint of flare-to-flare S/Si variability in our data (Table 3), perhaps reflecting different "ages" of the regolith in the different sampled regions.

The preceding discussion raises the important issue of surface *vs.* bulk composition: how confident can we be that the composition of the surface determined by the XRS is representative of the bulk asteroid? Eros is covered with a sizeable and complex regolith (Veverka *et al.*, 2001). This regolith is probably made up of material fragmented by the numerous impacts that have marred the asteroid's surface, and it is thus highly probable that its bulk composition is representative of the underlying bedrock. However, several physical processes could in principle lead to compositional heterogeneity within the regolith, in addition to the surface processes described above. These include size-sorting mechanisms, for example the "Brazil nut problem", wherein large grains rise to the surface of a shaken mixture of different sized hard spheres (Rosato *et al.*, 1987), the reverse Brazil nut problem in which the larger grains sink (Hong *et al.*, 2001), or photoelectric levitation and redistribution of small grains (Lee, 1996; Robinson *et al.*, 2001). If different minerals have different grain size distributions within the regolith, size-sorting processes like these could cause compositional variability, either with depth or in different spatial regions. The most likely component to be significantly fractionated within the regolith by such processes is Fe-Ni metal, since its material properties are so different from the silicates that dominate the mixture.

In terms of the XRS, regolith sorting of metal and silicates could (1) increase the surface Fe/Si ratio if metal is segregated to the surface, (2) decrease Fe/Si if metal grains sink, or (3) lead to Fe/Si spatial heterogeneity across the asteroid. The XRS results do not provide evidence for spatial variability in the Fe/Si ratio, but systematic errors preclude this being a very firm result. Our data favor an Fe/Si ratio similar to that of H or R chondrites (Fig. 13). If Fe-Ni metal is preferentially concentrated at the regolith surface, the "true" bulk composition of Eros would have lower iron abundance, perhaps similar to L or LL chondrites. On the other hand, sinking of metal would indicate a bulk Fe abundance higher than any known ordinary chondrites.

A possible indication of small-scale metal-silicate separation is provided by preliminary results from the NEAR GRS (Evans *et al.*, 2001). Analyses of gamma-ray spectra acquired from the surface of Eros indicate an Fe/Si ratio lower than that determined by the XRS and an Fe/O ratio considerably lower than bulk chondrites. These data sample a small region of the asteroid, probably a "ponded" deposit within a crater (Veverka *et al.*, 2001b). The lower apparent iron abundance from these measurements compared with the orbital XRS data suggests that this localized area has indeed been depleted in metal (see also McCoy *et al.*, 2001), relative to a bulk ordinary chondrite composition. This is consistent with the suggestion by Robinson *et al.* (2001) that the "ponds" observed by the NEAR MSI on Eros are preferentially composed of fine-grained material, perhaps segregated by photoelectric-induced levitation. Finally, we note that the XRS data do not distinguish between H and R chondrites. However, despite having similar bulk iron abundances, R chondrites are much more oxidized than H chondrites and have essentially no metal (Kallemeyn *et al.*, 1996). Thus, if the differences in apparent iron abundance determined by the XRS and GRS are due to regolith sorting of metal and silicates, this would argue against an Eros-R chondrite link.

CONCLUDING REMARKS

We have presented elemental ratios (Mg/Si, Al/Si, S/Si, Ca/Si, and Fe/Si) of the surface of the S-class asteroid 433 Eros, measured with the NEAR XRS. Errors in the determination of the incident solar x-ray spectra from measurements with the NEAR solar monitor lead to a large overall uncertainty in the Ca/Si and Fe/Si ratios. However, the Fe/Ca ratio is much more certain and is closely similar to ordinary chondrites. Because the Mg/Si and Al/Si ratios also appear chondritic, we argued that the Fe/Si and Ca/Si ratios are probably chondritic as well and the few data points that are discrepant are artifacts of errors in determining solar spectra. Assuming that this is the case, and averaging our results acquired during five solar flares and two extended periods of quiet Sun, we have determined the average bulk composition of the surface of Eros. The salient features of this composition and the conclusions we draw can be summarized as follows:

(1) Mg/Si, Al/Si and Ca/Si ratios indicate that Eros has not been globally differentiated into a core, mantle and crust.

(2) The very low S/Si ratio indicates that sulfur has been depleted from an initially chondritic composition. This depletion was likely caused by surface devolatalization and loss of sulfur, due to meteor impacts and/or photo- or ion-induced sputtering. Alternatively, a limited degree of partial melting and loss of an FeS-rich partial melt could deplete the sulfur abundance. We think this is less likely than the surface devolatalization scenario, both because no meteorites with S depletions but chondritic Mg, Al and Ca are known and because such melting would be expected to lead to spatial compositional heterogeneity more extensive than allowed by our data (*e.g.*, McCoy *et al.*, 2000).

(3) Our derived Fe/Si ratio is most consistent with H or R chondrites. However, systematic errors in modeling solar spectra and modeling x-ray spectra from mixtures of minerals are large and the lower iron ordinary chondrite subclasses L and LL could be consistent with our data if we consider the total Fe/Si error budget. Adding additional uncertainty is the possibility of metal-silicate segregation in the asteroid's regolith. Various sifting and sorting processes could deplete or enrich the surface in Fe-Ni metal. Thus, determining the true bulk Fe/Si ratio of Eros, to distinguish between H, L and LL ordinary chondrite subclass for instance, is probably not possible from remote-sensing data.

The results presented here demonstrate that remote-sensing XRS can provide important compositional information about planetary surfaces. However, one of the great strengths of the NEAR–Shoemaker mission is the complementary information

provided by a battery of different scientific instruments. Synthesizing the data from the XRS with results from the MIS, NIS and GRS can potentially provide more stringent constraints on the origin and history of Eros. Such a synthesis is presented by McCoy *et al.* (2001).

Acknowledgements–The authors acknowledge the extraordinary efforts of the NEAR-Shoemaker mission design and mission operations teams and the science data center at Johns Hopkins University/Applied Physics Laboratory for making the collection of x-ray data from Eros possible. We also thank the NEAR MSI team for sharing the mosaic used in Fig. 1 and Hap McSween and Ed Scott for helpful reviews. L. R. N. would like to thank J. Nuth and R. Vondrak of Goddard Space Flight Center for their interest and support.

Editorial handling: D. W. G. Sears

REFERENCES

ADLER I. *ET AL.* (1972a) Apollo 15 geochemical x-ray fluorescence experiment: Preliminary report. *Science* **175**, 436–440.

ADLER I. *ET AL.* (1972b) The Apollo 15 x-ray fluorescence experiment. *Proc. Lunar Sci. Conf.* **3rd**, 2157–2178.

ADLER I. *ET AL.* (1972c) Apollo 16 geochemical x-ray fluorescence experiment: Preliminary report. *Science* **177**, 256–259.

ANTONUCCI E. AND MARTIN R. (1995) Differential emission measure and iron-to-calcium abundance in solar flare plasmas. *Astrophys. J.* **451**, 402–412.

BRADLEY J. P., SANDFORD S. A. AND WALKER R. M. (1988) Interplanetary dust particles. In *Meteorites and the Early Solar System* (eds. J. F. Kerridge and M. S. Matthews), pp. 861–895. Univ. Arizona Press, Tucson, Arizona, USA.

CHAPMAN C. R. (1996) S-type asteroids, ordinary chondrites, and space weathering: The evidence from *Galileo's* fly-bys of Gaspra and Ida. *Meteorit. Planet. Sci.* **31**, 699–725.

CHENG A. F. (1997) Near-Earth asteroid rendezvous: Mission overview. *Space Sci. Rev.* **82**, 3–29.

CINTALA M. J. (1992) Impact-induced thermal effects in the lunar and mercurian regoliths. *J. Geophys. Res.* **97**, 947–973.

CLARK P. E. (1979) Correction, Correlation, and Theoretical Consideration of Lunar x-ray Fluorescence Intensity Ratios. Ph.D. thesis, University of Maryland, College Park, Maryland, USA. 136 pp.

CLARK P. E. AND TROMBKA J. I. (1997) Remote x-ray spectrometry for NEAR and future missions: Modeling and analyzing x-ray production from source to surface. *J. Geophys. Res.* **102**, 16 361–16 384.

CLARK P. E., TROMBKA J. I. AND FLOYD S. (1995) Solar monitor design for the NEAR x-ray spectrometer (abstract). *Lunar Planet. Sci.* **26**, 253–254.

ERICKSON J. E. (1968) Velocity distribution of sporadic meteors. *J. Geophys. Res.* **73**, 3721–3726.

EVANS L. E., STARR R. D., BRUCKNER J., REEDY R. C., BOYNTON W. V., TROMBKA J. I., GOLDSTEN J. O. AND MASARIK J. (2001) Elemental composition from gamma-ray spectroscopy of the NEAR-Shoemaker landing site on 433 Eros. *Meteorit. Planet. Sci.* **36**, 1639–1660.

FELDMAN U., DOSCHEK G. A., BEHRING W. E. AND PHILLIPS K. J. H. (1996) Electron temperature, emission measure, and x-ray flux in A2 to X2 x-ray class solar flares. *Astrophys. J.* **460**, 1034–1041.

GAFFEY M. J., BURBINE T. H. AND BINZEL R. P. (1993a) Asteroid spectroscopy—Progress and perspectives. *Meteoritics* **28**, 161–187.

GAFFEY M. J., BURBINE T. H., PIATEK J. L., REED K. L., CHAKY D. A., BELL J. F. AND BROWN R. H. (1993) Mineralogical variations within the S-type asteroid class. *Icarus* **106**, 573–602.

GARCIA H. A. (1994) Temperature and emission measure from GOES soft x-ray measurements. *Solar Phys.* **154**, 275–308.

GOLDSTEN J. O. *ET AL.* (1997) The x-ray/gamma-ray spectrometer on the near-Earth asteroid rendezvous mission. *Space Sci. Rev.* **82**, 169–216.

HONG D. C., QUINN P. V. AND LUDING S. (2001) The reverse Brazil nut problem: Competition between percolation and condensation. *Phys. Rev. Lett.* **86**, 3423–3426.

HUBBELL J. (1969) Photon cross-sections, attenuation coefficients, and energy absorption coefficients from 10 keV to 100 GeV. Rep. NSRDS-NBS **29**, Nat. Bur. Stand., Washington D.C., USA. 80 pp.

HUBBELL J. H. AND SELTZER S. M. (1997) Tables of x-ray mass attenuation coefficients and mass energy-absorption coefficients. National Institute of Standards and Technology, Gaithersburg, Maryland, USA.

HUBBELL J. H., VEIGELE W. J., BRIGGS E. A., BROWN R. T., CROMER D. T. AND HOWERTON R. J. (1975) Atomic form factors, incoherent scattering functions, and photon scattering cross sections. *J. Phys. Chem. Ref. Data* **4**, 471–538.

JENKINS R. AND DEVRIES J. (1969) *Practical X-Ray Spectrometry*. Springer-Verlag, New York, New York, USA. 189 pp.

KALLEMEYN G. W., RUBIN A. E. AND WASSON J. T. (1996) The compositional classification of chondrites: VII. The R chondrite group. *Geochim. Cosmochim. Acta* **60**, 2243–2256.

KERRIDGE J. F. AND MATTHEWS M. S., EDS. (1988) *Meteorites and the Early Solar System*. Univ. Arizona Press, Tucson, Arizona, USA. 1269 pp.

KILLEN R., POTTER A. E., REIFF P., SARANTOS M., JACKSON B. V., HICK P. AND GILES B. (2001) Evidence for space weather at Mercury (abstract). *J. Geophys. Res.* **106**, E12.

KRAUSE M. O. (1979) Atomic radiative and radiationless yields for *K* and *L* shells. *J. Phys. Chem. Ref. Data* **8**, 307–327.

KULLERUD G. (1963) The Fe-Ni-S system. *Ann. Rep. Geophys. Lab* **67**, 4055–4061.

LEE P. (1996) Dust levitation on asteroids. *Icarus* **124**, 181–194.

LUCEY P. G., HINRICHS J. L., URQUHART-KELLY M., WELLNITZ D., BELL J. F., III AND CLARK B. E. (2001) Thermo-reflectane spectra of Eros: Unambiguous detection of olivine (abstract). *Lunar Planet. Sci.* **32**, #1490, Lunar and Planetary Institute, Houston, Texas, USA (CD-ROM).

MARQUARDT D. W. (1963) An algorithm for the estimation of non-linear parameters. *Soc. Ind. Appl. Math. J.* **11**, 431–441.

MATSUNAMI N., YAMAMURA Y., ITIKAWA Y., ITOH N., MIYAGAWA S., MORITA K. AND SHIMIZU R. (1984) Energy dependence of the ion-induced sputtering yields of monatomic solids. *Atomic Data Nucl. Data Tables* **31**, 1–80.

MCCLANAHAN T. P. *ET AL.* (1999) Data processing for the near-Earth asteroid rendezvous (NEAR) x-ray and gamma-ray spectrometer (XGRS) ground system. In *Hard X-Ray, Gamma-Ray, and Neutron Detector Physics* (eds. R. B. James and R. C. Schirato), pp. 74–87. The International Society for Optical Engineering, Bellingham, Washington, USA.

MCCOY T. J., NITTLER L. R., BURBINE T. H., TROMBKA J. I., CLARK P. E. AND MURPHY M. E. (2000) Anatomy of a partially differentiated asteroid: A "NEAR"-sighted view of acapulcoites and lodranites. *Icarus* **148**, 29–36.

MCCOY T. J. *ET AL.* (2001) The composition of 433 Eros: A mineralogical–chemical synthesis. *Meteorit. Planet. Sci.* **36**, 1661–1672.

MELOSH H. J. (1989) *Impact Cratering: A Geologic Process*. Oxford Univ. Press, New York, New York, USA. 245 pp.

MEWE R., GRONENSCHILD E. H. B. M. AND VAN DEN OORD G. H. J. (1985) Calculated x-radiation from optically thin plasmas. V. Improved atomic data for n = 1–2 lines plus satellites from H- and He-like ions, 2l-nl' (n > or = 2) and 3l-nl' (n > or = 3)

transitions from Fe and Ni ions, and lines from Li to Ne isoelectronic sequences of elements C to Ca. *Astron. Astrophys. Suppl.* **62**, 197–254.

MEYER J-P. (1985) Solar-stellar outer atmospheres and energetic particles, and galactic cosmic rays. *Astrophys. J. Suppl.* **57**, 173–204.

MITTLEFEHLDT D. W., MCCOY T. J., GOODRICH C. A. AND KRACHER A. (1998) Non-chondritic meteorites from asteroidal bodies. In *Planetary Materials* (ed. J. J. Papike), pp. 4-1 to 4-195. Mineralogical Society of America, Washington, D.C., USA.

MORGAN T. H. AND KILLEN R. M. (1998) Production mechanisms for faint but possibly detectable coronae about asteroids. *Planet Space Sci.* **46**, 843–850.

NITTLER L. R., CLARK P. E., MCCOY T. J., MURPHY M. E. AND TROMBKA J. I. (2000) Bulk compositional trends in meteorites: A guide for analysis and interpretation of NEAR XGRS data from asteroid 433 Eros (abstract). *Lunar Planet. Sci.* **31**, #1711, Lunar and Planetary Institute, Houston, Texas, USA (CD-ROM).

PIERAZZO E., VICKERY A. M. AND MELOSH H. J. (1997) A reevaluation of impact melt production. *Icarus* **127**, 408–423.

PIETERS C. M. *ET AL.* (2000) Space weathering on airless bodies: Resolving a mystery with lunar samples. *Meteorit. Planet. Sci.* **35**, 101–107.

RAYMOND J. C. AND SMITH B. W. (1977) Soft x-ray spectrum of a hot plasma. *Astrophys. J. Suppl.* **35**, 419–439.

ROBINSON M. S., THOMAS P. C., VEVERKA J., MURCHIE S. AND CARCICH B. (2001) The nature of ponded deposits on Eros. *Nature* **413**, 396–400.

ROSATO A., STRANDBURG K. J., PRINZ F. AND SWENDSEN R. H. (1987) Why the Brazil nuts are on top: Size segregation of particulate matter by shaking. *Phys. Rev. Lett.* **58**, 1038–1040.

SYLWESTER J., LEMEN J. R., BENTLEY R. D., FLUDRA A. AND ZOLCINSKI M-C. (1998) Detailed evidence for flare-to-flare variations of the coronal calcium abundance. *Astrophys. J.* **501**, 397–407.

STARR R. *ET AL.* (2000) Instrument calibrations and data analysis procedures for the NEAR x-ray spectrometer. *Icarus* **147**, 498–519.

THOMAS R. J., CRANNELL C. J. AND STARR R. (1985) Expressions to determine temperatures and emission measures for solar x-ray events from GOES measurements. *Solar Phys.* **95**, 323–329.

TROMBKA J. I. *ET AL.* (1997) Compositional mapping with the NEAR x-ray/gamma-ray spectrometer. *J. Geophys. Res.* **102**, 23 729–23 750.

TROMBKA J. I. *ET AL.* (2000) The elemental composition of asteroid 433 Eros: Results of the NEAR–Shoemaker x-ray spectrometer. *Science* **289**, 2101–2105.

VEVERKA J. *ET AL.* (2000) NEAR at Eros: Imaging and spectral results. *Science* **289**, 2088–2097.

VEVERKA J. *ET AL.* (2001a) Imaging of small-scale features on 433 Eros from NEAR: Evidence for a complex regolith. *Science* **292**, 484–488.

VEVERKA J. *ET AL.* (2001b) The landing of the NEAR-Shoemaker spacecraft on asteroid 433 Eros. *Nature* **413**, 390–393.

WETHERILL G. W. (1985) Asteroidal source of ordinary chondrites. *Meteoritics* **20**, 1–22.